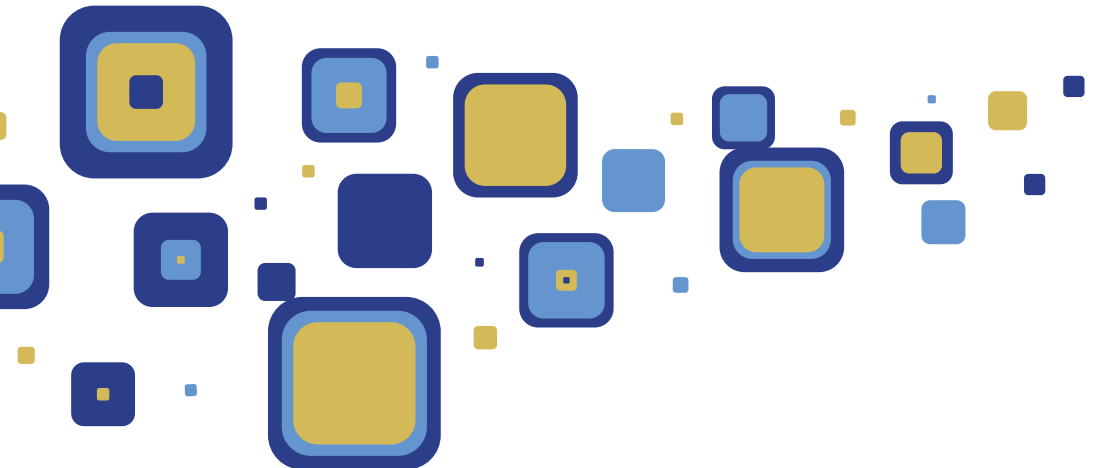


# CAL POLY

HONORS UNDERGRADUATE  
RESEARCH JOURNAL 2009



VOLUME TWO

# CAL POLY

## HONORS UNDERGRADUATE RESEARCH JOURNAL 2009

VOLUME TWO

UNIVERSITY HONORS PROGRAM  
CALIFORNIA POLYTECHNIC STATE UNIVERSITY  
SAN LUIS OBISPO, CALIFORNIA



# TABLE OF CONTENTS

Letter from the Director .....	7
Uses of Marine Compounds: Extraction and Chemical Profiling of a Caribbean Marine Sponge <i>Clathria</i> sp. <b>Dr. Jennifer Carroll</b> , Jenna Arruda .....	11
BalloonSat: Design, Implementation, and Application of a Low-cost Tethered Weather Balloon Remote Sensing Station <b>Dr. John Saghri</b> , Dustin Blackwell, John Hupton, Robert Hursig, Jessica Kiefer, Matt Schlutz, Scott Seims .....	27
Reproductive Life History and the Effects of Sex and Season on Morphology in <i>Crotalus oreganus</i> (Northern Pacific Rattlesnakes) <b>Dr. Emily N. Taylor</b> , Benjamin Kwittken .....	49
Simulations of the Polarization Dependence of the Light Potential Equation in Quantum Computing <b>Dr. Katharina Gillen</b> , Bert David Copsy .....	61
Rapid Detection of Total and Pathogenic <i>Vibrio parahaemolyticus</i> using Real-Time PCR with TaqMan® Fluorescent Probes <b>Dr. Marie Yeung</b> , Evan Markegard .....	71
Drop Impact Dynamic Response Study of JEDEC JESD22-B111 Test Board <b>Dr. Jianbiao Pan</b> , Michael Krist, Andrew Farris, Nicolas Vickers .....	81
The Expression of Alkaline Phosphatase in Colonial Ascidiarians <b>Dr. Elena Keeling</b> , Heidi Swangler, Katherine Januszewicz .....	99

## **Dedication**

This volume of the Honors Undergraduate Research Journal is dedicated to Ed Sullivan (1944-2009), Associate Dean of the College of Engineering.

## **Special thanks to the supporters of the University Honors Program:**

Susan Opava, *Dean of Research and Graduate Programs*

Phil Bailey, *Dean of the College of Science and Mathematics*

Mohammad Noori, *Dean of the College of Engineering*

David Wehner, *Dean of the College of Agriculture, Food and Environmental Sciences*

Linda Halisky, *Dean of the College of Liberal Arts*

## **EDITORIAL BOARD**

Sema E. Alptekin, *Managing Editor, Director of Honors Program*

Jennifer Merriam, *Assistant Editor, Production Chair*

## **Proposal Review Committee**

Susan Opava, *Dean of Research and Graduate Programs*

Ed Sullivan, *Associate Dean of the College of Engineering*

## **Faculty Review Board**

Matthew Burd

Saeed Niku

Christina Firpo

John Pan

Kat Gillen

John Saghri

Elena Keeling

Brian Self

Nilanjan Mitra

Christine Strand

José Montelongo

Marie Yeung

William Murray

Xiao-Hua Yu

**Printed by University Graphic Systems**, a student-run printing enterprise



UNIVERSITY GRAPHIC SYSTEMS  
CAL POLY'S STUDENT-RUN PRINTING ENTERPRISE

# LETTER FROM THE DIRECTOR OF THE UNIVERSITY HONORS PROGRAM

Intellectual creativity and exploration are the hallmarks of our Honors Program. The Honors Program builds relationships among all colleges on campus and seeks to educate students in the connections between the disciplines, from Engineering to English, Agriculture to Art, or Business to Biology.

What better way to experience “intellectual creativity and exploration” than to work closely with a professor and other students on an interdisciplinary undergraduate research project? The model that was developed in 2006 as part of the deliverables for a National Science Foundation grant has grown since both in quality and quantity. The number of research projects increased from 20 to 27, and the number of students who receive NSF scholarships increased from 21 to 30 over the past three years. The infrastructure of the Honors Program makes it possible to transcend some of the cross-college challenges that typically emerge in the administration of interdisciplinary efforts as students are matched with the faculty projects.

While the National Science Foundation (NSF) Scholarships in Science, Technology, Engineering, and Mathematics (S-STEM) grant provided scholarships to students participating in these research projects, institutional funds were given to faculty to support the projects they undertook with the students. I feel it is important to acknowledge all of those who supported this program with matching funds and their enthusiastic leadership. This includes Susan Opava, Dean of Research and Graduate Programs; Phil Bailey, Dean of the College of Science and Mathematics; Mohammad Noori, Dean of the College of Engineering; David Wehner, Dean of the College of Agriculture Food and Environmental Sciences, and Linda Halisky, Dean of the College of Liberal Arts. I would also like to send special thanks to Bill Durgin for his leadership in promoting research at our university during his tenure as the Provost.

The second volume of the Honors Undergraduate Research Journal contains peer-reviewed articles — just a small sample of the outstanding undergraduate research that took place in the 2007–2008 academic year. I would like to recognize the students and research faculty who participated in this program and submitted and reviewed papers for inclusion in this journal. I would also like to acknowledge all of the faculty mentors who made these research opportunities available for the students. Their time and efforts are evident in the work high-

lighted in these papers. Without their support, Cal Poly's Honors Undergraduate Research Program would not have been possible.

This volume is dedicated to the memory of Ed Sullivan (1944-2009), Associate Dean of the College of Engineering, who served as a member of the selection committee making the research funding decisions for the past three years. Ed's leadership and the technical expertise provided the tools for the committee to have a fair distribution of funds among the various Colleges and projects. But what made his contributions most valuable was his willingness and ability to recognize and support non-engineering as well as engineering projects — especially those with the potential to benefit the society as a whole. He will be terribly missed.

Although the research program was originally designed to provide opportunities for those who are already in the Honors Program, it has also become a very effective recruitment tool for the Honors Program. Participation in this Honors Undergraduate Research Program is available not only to Honors students, but to all students on campus with a desire to engage in undergraduate research. Many new students decided to join the Honors Program once they became aware of the research opportunities.

The feedback from students has been very positive. One student commented, "It's made me really proud to be a part of the Honors Program that gets undergraduates researching." We are already receiving feedback from prior year participants that the experience was both valuable and an excellent addition to their resumes, helping to distinguish them in job and graduate school applications.

This volume's editor is one of our very own Honors students, a contributor to the previous volume of this journal, Jennifer Merriam. She has also provided valuable assistance in the development of the Honors Undergraduate Research Program, including activities from proposal writing to assessment of the research program and analyzing results. Special thanks also go out to Cheri Baumgarten for all her tireless efforts in mentoring and advising students on research project availability and selection.

As in the past, this effort has been both rewarding and enriching for me personally, and I believe for all the students and faculty involved. In light of the current budget uncertainty, we are hopeful that we will be able to continue this beneficial program in the coming years.

Sema Alptekin, Director of the University Honors Program  
Managing Editor, Honors Undergraduate Research Journal

HONORS UNDERGRADUATE  
RESEARCH PAPERS

# USES OF MARINE COMPOUNDS: EXTRACTION AND CHEMICAL PROFILING OF A CARIBBEAN MARINE SPONGE *CLATHRIA* SP.

Jenna Arruda, Student Author  
Dr. Jennifer Carroll, Research Advisor

## ABSTRACT

The purpose of this research project is to identify and chemically profile active extracts of a marine sponge, *Clathria* sp., collected from St. Thomas, US Virgin Islands. Previously, pteridine alkaloids, sterol sulfates, and bromine-containing amides collected from various species of *Clathria* have shown anti-microbial and anti-cancer activities [1]. Sponge extracts were isolated through a combination of liquid-liquid extractions, adsorption silica-gel column chromatography and high-pressure liquid chromatography (HPLC). These extracts were tested for cytotoxicity and antifouling properties through an *Artemia* sp. lethality test and

*Bugula neritina*, and *Balanus amphitrite* settlement biological assays. Chemical profiling was achieved through carbon and proton nuclear magnetic resonance spectroscopy (NMR) as well as low-resolution mass spectrometry. Three extracts were found to contain highly cytotoxic compounds, which should be explored further to determine their potential biomedical applications. One extract was found to contain anti-fouling properties and may hold industrial applications.

## INTRODUCTION & BACKGROUND

The goal of marine natural products research is to discover and harness the therapeutic potential of compounds bio-synthesized by marine organisms and their symbiotic microorganisms. Marine sponges, tunicates, soft-coral and algae have been shown to contain a wealth of novel compounds with high anti-bacterial, anti-tumor, anti-viral, anti-inflammatory and analgesic properties [2,3]. Sponges in particular are a rich source of marine secondary metabolites due to their relative abundance, ease of collection, and the structurally diverse classes of natural products they produce [4]. Additionally, the relatively high percentage of symbiotic microorganisms in marine sponges, which can be as high as 60 percent of the total body mass, produce a varied chemical profile based upon environmental and temporal changes [5]. These secondary metabolites serve as chemical cues for larval settlement and mating and as territorial markings to prevent fouling and invasion by competitors for otherwise defenseless, soft-bodied and sessile organisms [3,6]

In 2004, forty-two marine-derived natural products were in clinical or pre-clinical trials [3]. Countless applications for these compounds have been identified and explored, including: the inhibition of tumor cell growth, anti-viral activity against Hepatitis B, and the treatment of Alzheimer's disease [7-10]. The mechanisms by which the compounds work are similarly diverse. Discodermolide, a polyketide isolated in 1990 from the Caribbean sponge *Discodermia dissoluta* acts to inhibit tumor cell growth [8]. Eleutherobin, first isolated from the soft coral *Eleutherobia* sp. from Western Australia is also a potent cancer-cell inhibitor [11]. Both Discodermolide and Eleutherobin share a similar microtu-

bule-stabilizing anti-mitotic mechanism with Taxol, the current leading drug for Ovarian Cancer therapy, first isolated and characterized from the tissue of the Pacific Yew tree in 1962 [11,12]. Ecteinascidin 743 (Trabectedin), from the Caribbean tunicate *Ecteinascidia turbinata*, is in clinical use in Europe and Korea in the treatment of soft-tissue sarcoma [13]. Additionally, Trabectedin is in multiple phase II and III clinical trials for breast, ovarian, prostate, and various sarcoma cancers [13,14]. Aside from the possibilities as therapeutic agents, marine natural products are being investigated for potential use as industrial additives to prevent biofouling.

Marine growth on man-made, underwater structures costs the shipping industry millions of dollars yearly [15]. Currently many of the anti-fouling additives in commercial use contain heavy metals, which are toxic to non-target organisms and bioaccumulate in the food chain [15,16]. Algal and invertebrate marine sources naturally and selectively inhibit fouling. An example, a dibrominated cyclopeptide from the marine sponge *Geodia barretti* was recently found to inhibit settlement of barnacle larvae [17]. With natural products such as this as templates, new alternatives to the overly toxic compounds in use today could be employed to more safely and effectively control these problem organisms.

The sponge of interest in this project, a *Clathria* species, has previously been shown to contain novel pteridine alkaloids, sterol sulfates, and bromine-containing amides, including Clathsterol, Clathrin A-C, Pseudoanchynazine A-C, Clathriol, Clathrynamide A-C, Mirabilin G, Microcionamides A and B, and Clathryimins A and B [1,18-24]. Clathsterol, a sulfated sterol, has shown activity against human immunodeficiency virus type 1 (HIV-1) by inhibiting the reverse transcriptase enzyme. Investigation of the compound Clathrynamide A has revealed its ability to inhibit growth of human myeloid leukemia cells [1].

In general, the process leading to the discovery of a new natural product for pharmaceutical application entails: 1) preliminary biological assays, 2) chemical profiling, 3) identification of biologically active components, 4) in-depth biological screening, and 5) clinical trials. This project involves the first steps in the process, namely initial chemical profiling and biological assays to determine bio-

activity.

## METHODS

### Collection and Identification

A sponge sample was collected from Brewer's Bay, St. Thomas, US Virgin Islands (18°20' N 64°55' W) by SCUBA at a depth of 10 m in May of 2006. A voucher sample (no. 0609, Figure 1) was prepared and frozen. The sponge is upright with open tubes and has a pimpled surface and a tough and elastic texture. It has a grey-orange exterior and brown-orange interior in water and is beige in methanol. One to five cm oscules are visible, distributed around the top of the sponge. Initial field taxonomy suggests the sponge is a *Clathria* species, however, due to the complexity and sheer number of species of marine invertebrates, exact taxonomy is difficult to confirm.



**Figure 1.** Sponge sample 0609.

### Extraction and Isolation

The sample was transported to Cal Poly where it was thawed and partitioned following the Kupchan Isolation Scheme, Figure 2 [25]. A 1 kg sample was soaked in 100% methanol (MeOH) for a minimum of 24 h to extract the most polar compounds. The MeOH was decanted and reserved and the procedure was repeated two more times. The sample was then extracted with 100% dichloromethane ( $\text{CH}_2\text{Cl}_2$ ) in the same fashion to separate the non-polar compounds.

Solvent was removed *in vacuo* and the crude  $\text{CH}_2\text{Cl}_2$  extract was partitioned with a system of hexanes and 90% MeOH/ water ( $\text{H}_2\text{O}$ ). The crude MeOH fraction was partitioned between  $\text{CH}_2\text{Cl}_2$  and  $\text{H}_2\text{O}$ . Water-soluble compounds were further separated with t-butanol (t-BuOH) and  $\text{H}_2\text{O}$ . The  $\text{CH}_2\text{Cl}_2$  fraction was successively partitioned with a system of 90% MeOH/  $\text{H}_2\text{O}$  and hexanes followed by a 50% MeOH/  $\text{H}_2\text{O}$  mixture. In total, seven crude fractions were isolated: DMM, DMH, FD, FM, FH, WW, and WB.

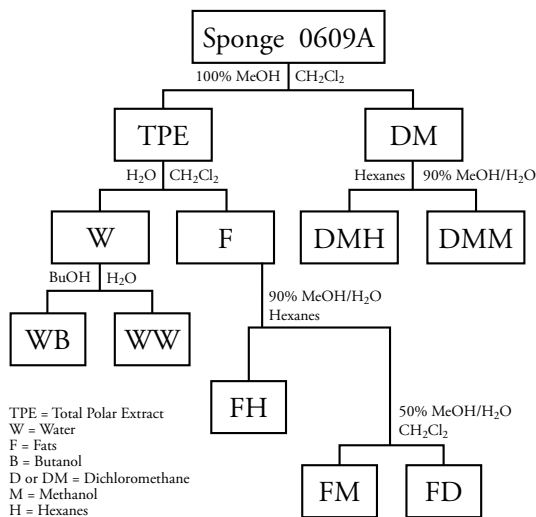


**Figure 2.** Kupchan Isolation Scheme

Further separation of crude extracts FD, FH, and DMH were accomplished as follows. Fractions FD and FH were combined due to similar composition according to  $^1\text{H}$  NMR data and the combined FD/FH extract was subjected to silica-gel column chromatography (eluted with a 10% v/v stepwise gradient of MeOH/  $\text{CH}_2\text{Cl}_2$ ) giving 5 fractions, FD/FH 1-5. FD/FH 4 was further separated into fractions A-F by column chromatography (eluted with a 10% stepwise gradient of EtOAc/ $\text{CH}_2\text{Cl}_2$ ). DMH was separated by flash silica-gel chromatography (10% stepwise gradient of EtOAc/heptanes), yielding five fractions, DMH 1-5. Figures 3 and 4 show the detailed isolation schemes.

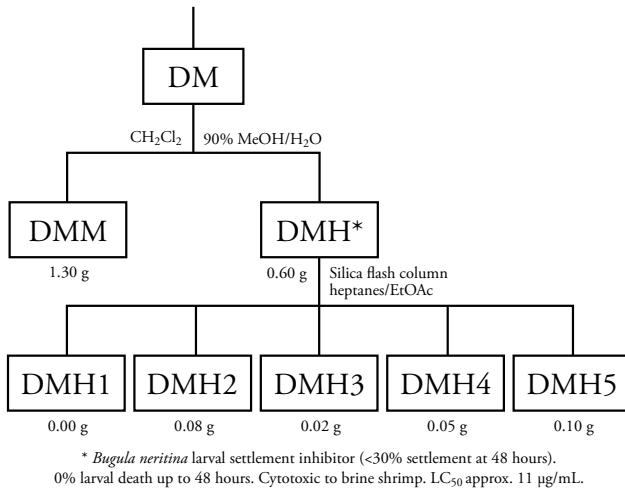


**Figure 3.** Isolation scheme from the crude dichloromethane (DM) extract. The weight of each fraction is shown below the respective box.

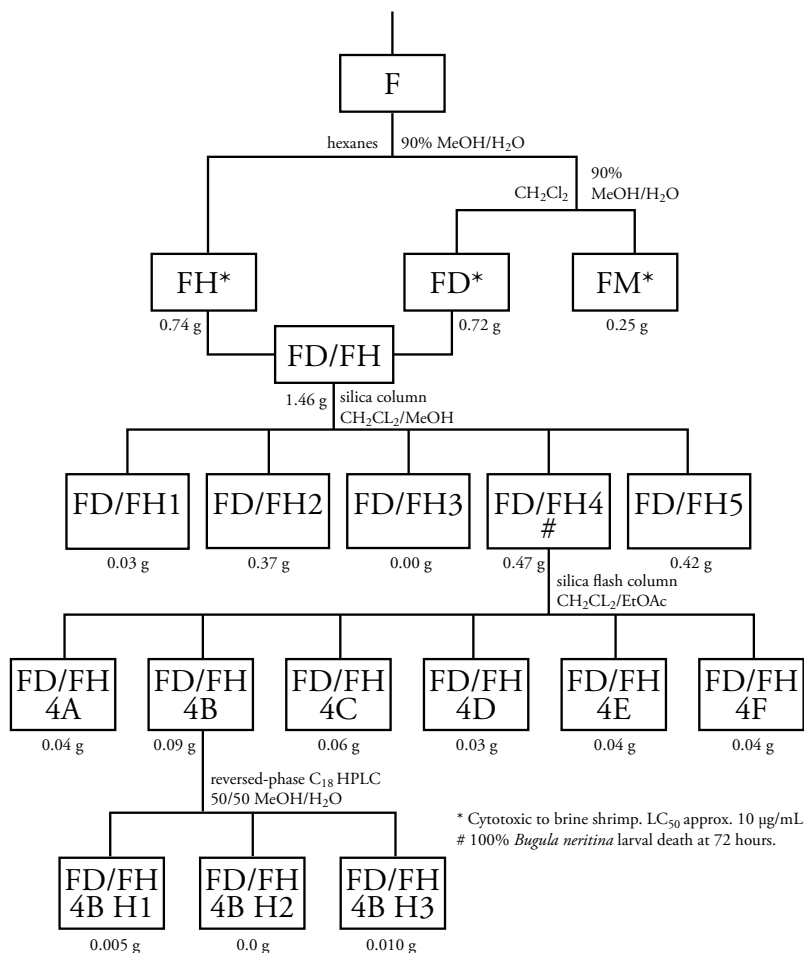


**Figure 4.** Isolation scheme from crude fats (F) extract.

All isolation steps were bioassay-guided, meaning that the purification of the most biologically active component was pursued. The bioassay results that dictated the isolation scheme are discussed later. NMR results also guided isolation, dependent on the presence or absence of key functional groups typical of other natural products. In some cases, such as the isolation of FD/FH 4B, sample mass dictated further purification – bioassays and complete purification of very small samples was not possible.

## Bioassays

A series of bioassays were performed to determine extract cytotoxicity (*Artemia* sp. lethality test) and anti-fouling properties (*Bugula neritina* and *Balanus amphitrite* settlement bioassays). For the *Artemia* sp. bioassay, cysts were hatched in a filtered seawater solution (FSW) at room temperature in a separatory funnel. A lamp was used to provide direct light and a fish-tank pump was used for an air source. Eggs were allowed to hatch for 48 h before harvesting. Five crude extracts (FD, FH, FM, DMM, and DMH) were tested for cytotoxicity at three concentrations: 15µg/mL, 10µg/mL, and 5µg/mL in di-methyl sulfoxide (DMSO), diluted to a total volume of 5 mL with FSW. Approximately 15 live *Artemia* sp. were added to each 10 mL glass test tube. Death rate was measured at 24 and 48-hour intervals. Experimental error was corrected for with DMSO and FSW controls. Results of the bioassay are summarized in Table 1. LC<sub>50</sub> values (concentration at which 50 percent death occurs) of each extract were determined by plotting the mortality rates against sample concentration (Figure 5). Fractions FD, FH, FM, and DMH all showed substantial levels of cytotoxicity. Fractions FD, FH, and DMH gave the most relevant LC<sub>50</sub> values within the concentration parameters. The LC<sub>50</sub> values for FD, FH, and DMH were roughly 13, 12, and 11 µg/mL, respectively.

**Table 1.** Percent mortality of *Artemia* sp. at 24 and 48 hour incubation times.

	% Mortality 24 Hours			% Mortality 48 Hours		
	5 µg/mL	10 µg/mL	15 µg/mL	5 µg/mL	10 µg/mL	15 µg/mL
DMM	0.0	0.0	0.0	0.0	0.0	90.9
DMH	0.0	0.0	0.0	0.0	27.3	100.0
FD	0.0	20.0	28.6	7.1	26.7	64.3
FM	0.0	50.0	81.3	66.7	57.1	100.0
FH	7.7	0.0	0.0	15.4	16.7	78.6
DMSO	0.0	0.0	0.0	0.0	0.0	0.0
FSW	0.0	0.0	0.0	0.0	0.0	0.0

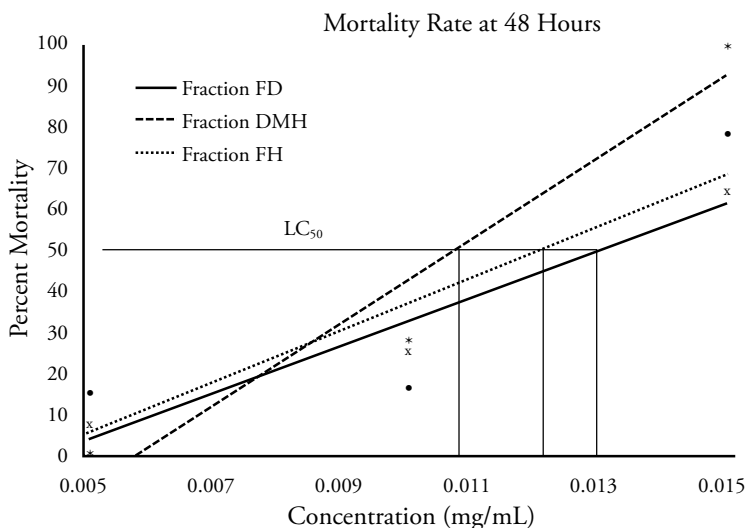


**Figure 5.** Mortality rate of *Artemia sp.* at varying extract concentration

A settlement bioassay was performed to determine the anti-fouling properties of the extracts. *Bugula neritina* larvae were collected from Morro Bay, CA and kept in the dark for 2 days. Larval release was induced by 2 hours of light exposure. Two-hundred  $\mu\text{L}$  aliquots of each extract were pipetted into a 96-well polystyrene tissue culture plate. One larva was placed into each well in a volume of 100  $\mu\text{L}$  sea water, to give a final extract concentration of 5 mg/mL. The tray was incubated at 15°C and monitored for settlement and death at 3, 24, 48, and 72 hours. Fractions FM, DMM, DMH, and FD/FH 2, 4, and 5 were tested in this assay. Fractions FD and FH had been combined, due to similar cytotoxicity and NMR spectra, and further separated into fractions FD/FH 1-5. Of those, fractions FD/FH 2, 4, and 5 were chosen for the settlement assay. Bioassay results are presented in Table 2 and a graph of percent settlement and percent death after 72 hours (Figure 6) was constructed to determine the efficacy of each extract as an anti-fouling agent. The graphs reveal that of the extracts tested, DMH shows both low mortality and low larval settlement, indicating a potential antifouling

candidate. Fraction FD/FH 4, seen in Figure 6, caused 100% larvae death at 72 hours, indicating poor antifouling activity but high cytotoxicity.

**Table 2.** Percent settlement and death of *Bugula neritina* at 3, 24, 48 and 72 hours.

	3 hours		24 hours		48 hours		72 hours	
	% Settled	% Dead						
DMSO	0.0	0.0	33	0.0	33	25	33	67
FSW	8.0	0.0	67	0.0	100	17	100	42
FM	25	0.0	25	0.0	100	50	100	83
DMH	25	0.0	33	0.0	33	0.0	25	25
DMM	0.0	0.0	25	0.0	42	25	42	67
FD/FH 2	33	0.0	50	0.0	58	8.0	58	50
FD/FH 4	25	0.0	25	0.0	50	42	100	100
FD/FH 5	67	0.0	75	0.0	100	8.0	67	33

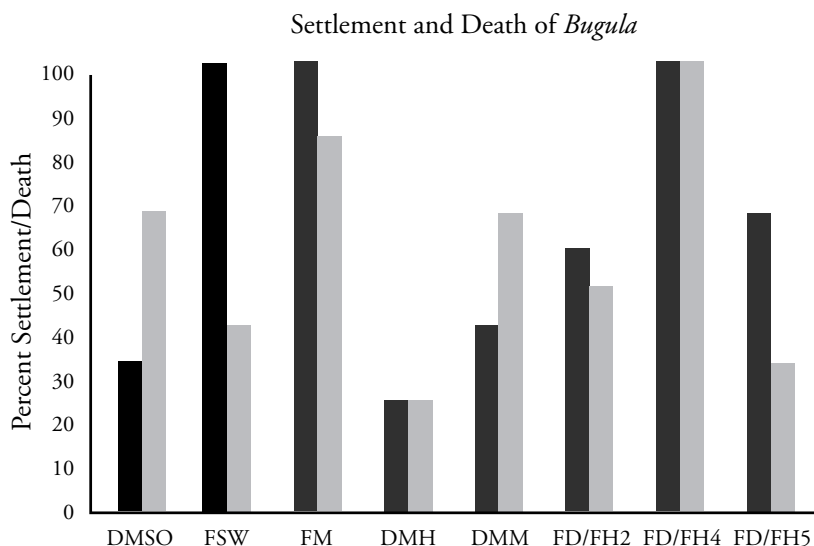


**Figure 6.** Percent settlement and percent death of *Bugula neritina* larvae in each of five extracts after 72 hours.

Due to promising anti-settlement activity, sub-fractions of crude extract DMH were isolated and tested. The *Bugula neritina* bioassay was unrepeatable

due to a larvae shortage, so a *Balanus amphitrite* bioassay was employed to carry out further anti-settlement tests. Barnacle cypris larvae were received from Duke University and held at 4°C. The larvae were warmed by a light source for thirty minutes prior to use to activate the cyprids. A pipette was used to transfer one larva into each well of a 96-well plate with sponge extracts previously added. Each larva was added in a volume of 100 µl, giving a final extract concentration of 1.0 mg/mL. The tray was incubated at 25°C and observed at 3, 24, 48 and 72 hours. At each observation the larvae were recorded as alive/active, dead, or metamorphosed into a juvenile barnacle. Results of the bioassay are presented in Table 3 and Figure 7. All tested fractions showed strong anti-settlement properties and Fractions DMH 2-4 also showed high cytotoxicity.

**Table 3.** Percent settlement and death of *Balanus amphitrite* at 3, 24, 48 and 72 hours.

	3 hours		24 hours		48 hours		72 hours	
	% Settled	% Dead						
DMH	0	0	0	0	0	0	0	0
DMH 1	0	0	0	0	0	0	0	0
DMH 2	0	0	0	17	0	100	0	100
DMH 3	0	0	0	100	0	100	0	100
DMH 4	0	100	0	100	0	100	0	100
DMH 5	0	0	0	0	0	0	0	25
DMSO	0	0	8	0	17	0	33	0
FSW	0	0	50	0	58	0	58	0

### Settlement and Death of *Balanus*

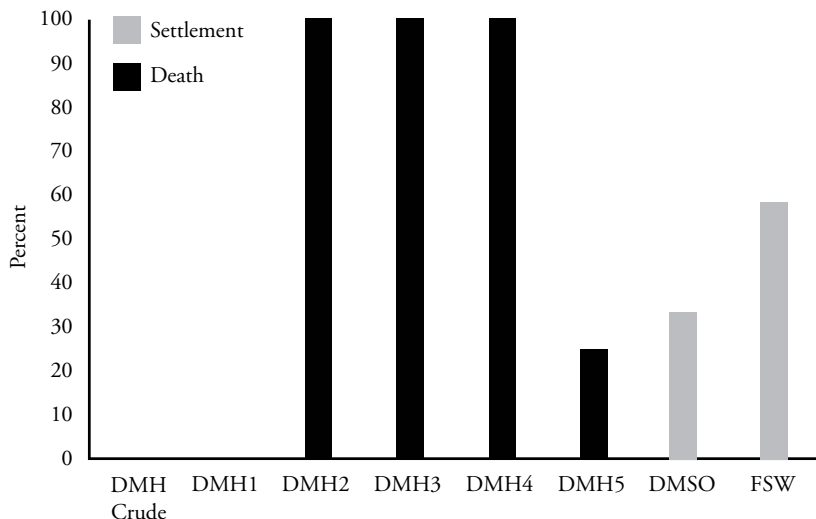


**Figure 7.** Percentage of *Balanus amphitrite* reached metamorphosis.

### Compound Identification

To determine composition of crude fractions, molecular weights were obtained by low-resolution mass spectrometry. A summary of key chemical shifts is presented in Table 4. Molecular weight results were compared with the literature values for compounds previously isolated from *Clathria* sp. A 270.3 g/mol natural product was identified in fraction FD/FH 5 that matches closely with Clathrin B, which has a molecular weight of 270.0 g/mol. Based on molecular weight alone, the presence of Clathrin B can neither be confirmed nor rejected. It is unlikely this compound is isolatable given such a low abundance according to the mass spectra. No other molecular weight matches were found.

**Table 4.** Mass spectrometry data of extracts, ordered by molecular weight.

Mass (m/z)	Intensity	Time (min)	Sample
212.20	35.50	17.74	FD/FH 3
226.00	6.00	1.88	FD/FH 5
226.00	5.00	11.13	FM
253.30	5.00	3.24	DMM
264.10	14.00	1.72	DMM
264.10	19.00	1.72	FD/FH 5
270.30	24.70	12.92	FD/FH 5
278.20	110.20	19.75	FD/FH 3
278.30	10.20	19.80	FD/FH 1
278.30	13.60	19.75	FD/FH 2
294.30	13.30	11.29	FD
312.20	20.80	19.38	DMH
337.40	11.00	17.69	FD/FH 2
337.40	12.00	19.34	FD/FH 5
343.40	48.90	17.90	FD/FH 4C
384.40	23.00	19.97	FD/FH 4
398.30	1176.30	19.27	FD/FH 4C
398.30	3546.70	19.32	FD/FH 4D
451.40	114.60	18.74	FD/FH 4C
457.50	4.40	20.17	FD/FH 2
479.40	613.90	17.18	FD
479.40	405.20	17.28	FM
481.40	15.50	13.54	DMM
481.40	9.00	13.59	FD/FH 1
493.40	6.00	19.50	FD
509.50	32.10	16.80	DMH
509.50	16.30	17.90	DMH

Proton and carbon NMR spectra were taken of every fraction and compared with published chemical shift values of the known compounds from *Clathria* sp. Comparing chemical shift values helps to determine the presence of similar chemical structures and functional groups between the literature compounds and those isolated from sample 0609. Additionally, molecular weights from mass spectra were searched in MarinLit software and compound hits were compared with corresponding  $^1\text{H}$  and  $^{13}\text{C}$  NMR to confirm the presence or absence of

previously discovered marine natural products. Neither the comparison of NMR spectra or the MarinLit search yielded any compound matches.

## DISCUSSION

### **Therapeutic Potential**

Based on results of the *Artemia* sp. lethality test, fractions FD, FH, and DMH are the most promising extracts in terms of potential medicinal applications. LC<sub>50</sub> values of these extracts against *Artemia* sp. ranged from 11 to 13 µg/mL. Assay results are not directly comparable when different model organisms are used but, to give these results a little perspective, Clathriol, previously isolated from a *Clathria* species was found to inhibit histamine release in peritoneal mast cells by 72 percent and inhibit the activation of human peripheral blood neutrophils by 76 percent at a concentration of 30 µM (14.4 µg/mL) [20]. Another compound previously isolated from a *Clathria* species, Microcionamide B, showed cytotoxicity toward two human breast tumor cell lines with LC<sub>50</sub> values of 177 and 172 nM (0.155 and 0.151 µg/mL, respectively) [23]. Further biological testing of these extracts should be pursued on other organisms or cell lines to further explore their bioactivity.

### **Anti-fouling Potential**

Results of the *Bugula neritina* bioassay suggest that fraction DMH is the most promising anti-fouling candidate. A subsequent assay with *Balanus amphitrite* barnacles further confirms that the crude DMH fraction and all sub-fractions have anti-fouling properties; all of these fractions showed 100 percent inhibition of settlement and metamorphosis while controls did not yield similar results. The ideal anti-fouling compound has both strong anti-settlement properties and low cytotoxicity. In this way, the compound works to prevent unwanted growth by other organisms without being toxic to the surrounding environment. For example, a boat coating containing anti-fouling components should prevent barnacle growth but not be toxic to other marine life. Fractions DMH 2, 3, and 4 all showed high cytotoxicity and should be re-tested at lower concentrations to determine if anti-fouling properties are retained at lower cytotoxicities. DMH 1,

on the other hand, appears to be a good anti-fouling candidate at the test concentration of 1.0 mg/mL.

### Chemical Profiling

$^1\text{H}$ ,  $^{13}\text{C}$ , and mass spectrometry data were reviewed and compared with literature reports of each of the compounds previously isolated from *Clathria*, however none of the known compounds were found in the examined fractions of sponge 0609. A lack of repeatable compound isolation might suggest that initial field taxonomy is incorrect and 0609 is not a *Clathria* sp. Furthermore, the fact that no matches were found through the MarinLit database suggests that the major compounds found in the 0609 extracts have not previously been identified or catalogued.

Complete structure elucidation was not feasible due to difficulties purifying extracts primarily because of very small sample size. The compounds closest to being pure FD/FH 4B H1-3 were not available in masses adequate to obtain a  $^1\text{H}$  or  $^{13}\text{C}$  NMR spectra. The largest of these fractions was 10 mg and was still insufficient for structure elucidation.

If further isolation were pursued it would be worthwhile to attempt to further separate fraction DMH 2 or DMH 4. Crude fraction DMH showed the best anti-settlement properties and sub-fractions 2 and 4 hold the compounds with the largest masses and most interesting functional groups as seen by NMR.

## ACKNOWLEDGEMENTS

Department of Chemistry and Biochemistry, College of Science and Math College-Based Fees, NSF DUE-631113, Dean Wendt and Lenora Brewer (Cal Poly Biology Department)

## WORKS CITED

1. Rudi, A., Yosief, T., Loya, S., Hizi, A., Schleyer, M., Kashman, Y. *J. Nat. Prod.* 2001, 64, 1451-1453.
2. Ireland, C.M., Roll, D. M., Molinski, T. F., Zarbriske, T. M., and Swersey, J. C. *California Academy of Sciences.* 1988, 41-58.
3. Newman, D. J., Cragg, G. M. *J. Nat. Prod.* 2004, 67, 1216-1238.

4. Carté, B. K. *BioScience*. 1996, 46, 271-276.
5. Lee, Y. K., Lee, J., Lee, H. K. J. *Microbiol.* 2001, 39, 254-264.
6. Zimmer, R. K. Butman, C. A. *Biol. Bull.* 2000, 198, 168-187.
7. Phase I/II Trial of KRN7000 in Patients with Chronic Hepatitis B Infection. Accessed April 11, 2008, from: <http://clinicaltrials.gov>
8. Florence, G. J., Gardner, N. M., Paterson, I. *Nat Prod Rev.* 2007, 25, 342-375.
9. Banerjee, S., Wang, Z., Mohammad, M., Sarkar, F., Mohammad, R. *J. Nat. Prod.* 2008, 71, 492-496.
10. Bryostatins Clinical Trials. Accessed May 18, 2008 from: <http://clinicaltrials.gov>
11. Long, B. H., Carboni, J., Wasserman, A., Cornell, L., Casazza, A., Jensen, P., Lindel, T., Fenical, W., Fairchild, C. *Cancer Research*. 1998, 58, 1111-1115.
12. Wall, M. E. *Cancer Research*. 1995, 55, 753-760.
13. S.Korea approves Zeltia cancer drug Yondelis, Accessed May 8, 2008 from, [www.reuters.com](http://www.reuters.com).
14. Carter, N. J., Keam, S. J. *Drugs*. 2007, 67, 2257-2276.
15. Braithwaite, R. A., McEvoy, L. A. *Adv Mar Biol.* 2005, 47, 215-252.
16. Bhattarai, H. D., Paudel, B., Park, N. S., Lee, K. S., Shin, H. W. *J Environ Biol.* 2007, 28, 857-863.
17. Hedner, E., Sjögren, M., Hodzic, S., Andersson, R., Göransson, U., Jonsson, P. R., Bohlin, L. *J. Nat Prod.* 2008, 71, 330-333.
18. Capon, R. J., Miller, M., Rooney, F. *J. Nat. Prod.* 2000, 63, 821-824.
19. Zuleta, I. A., Vitelli, M. L., Baggio, R., Garland, M. T., Seldes, A. M., Palermo, J. A. *Tetrahedron*. 2002, 58, 4481-4486.
20. Keyzers, R. A., Northcote, P. T., Webb, V. *J. Nat. Prod.* 2002, 65, 598-600.
21. Ohta, S., Okada, H., Oclarit, J. M., Ikegami, S. *Tetrahedron Letters*. 1993, 34, 5935-5938.
22. Capon, R. J., Miller, M., Rooney, F. *J. Nat Prod.* 2001, 64, 643-644.
23. Davis, R., Mangalindan, G., Bojo, Z., Antemano, R., Rodriguez, N., Concepcion, G., Samson, S., de Guzman, D., Cruz, L., Tasdemir, D., Harper, M. K., Feng, X., Carter, G., and Ireland, C. *J. Org. Chem.* 2004, 69, 4170-4176.
24. Sperry, S., Crews, P. *Tetrahedron Letters*. 1996, 37, 2389-2390.
25. Kupchan S. M., Tsou G. 1973, *J. Org. Chem.* 38: 178.

# BALLOONSAT: DESIGN, IMPLEMENTATION, AND APPLICATION OF A LOW-COST TETHERED WEATHER BALLOON REMOTE SENSING STATION

Dustin Blackwell, John Hupton, Robert Hursig, Jessica Kiefer,  
Matt Schlutz, Scott Seims, Student Authors  
Dr. John Saghri, Research Advisor

## ABSTRACT

Design, implementation, and applications of a low-cost tethered helium-filled weather balloon remote sensing station called BalloonSat is discussed. BalloonSat remote sensing station has been designed, implemented, and continuously upgraded and improved by Cal Poly students in the remote sensing course taught by Dr. John Saghri over the past few years. BalloonSat provides the raw multi-

spectral imagery data needed for a number of research projects. The onboard visible, infrared, and thermal sensors have wireless remote pan and zoom with real-time video monitoring capabilities. The collected remotely sensed data is transmitted to the ground station through a low-power wireless communication channel. Initial launches of the new and improved BalloonSat have demonstrated improved physical stability and wind-tolerance than previous designs. The collected multispectral data is exploited to provide useful information pertinent to the local terrain. The long term goal of this research is to develop digital image processing schemes to exploit the remotely sensed multispectral imagery collected by the BalloonSat in various applications useful for the campus and the surrounding community. The current application being investigated is the assessment of the status of the campus open parking lots. A robust image exploitation scheme has been successfully developed to identify and count vehicles in campus open parking lots. In the near future, with the recently added thermal imaging capability, more challenging and multi-sensor exploitation schemes will be developed for such applications as campus security, campus traffic monitoring, and campus tour.

## INTRODUCTION

Remote sensing is a challenging multidisciplinary science with numerous commercial and military applications. The objective of this research is to develop a low-cost tethered helium-filled weather balloon remote sensing station capable of collecting and exploiting multispectral imaging data from the local terrain for various civilian applications. The BalloonSat remote sensing station has been designed, implemented, and continuously upgraded and improved by Cal Poly students in the remote sensing course taught by Dr. John Saghri over the past few years. The system is comprised of a tethered helium-filled weather balloon and an aerial multispectral imaging platform. The aerial multispectral imaging system, or “payload,” consists of an upper box, which stores the electronics and batteries, a C-bracket which provided the stability for the panning motion, and a lower box which houses the two cameras, shortwave infrared lens and chang-

ing mechanism, and also a shutter release servo. The helium balloon is filled to about 8 feet in diameter and secured to the ground by four tethered lines. The two cameras and the interchangeable short wavelength infrared lenses provide an inexpensive multispectral imaging capability. The cameras have wireless remote pan and zoom with real-time video monitoring capabilities. The collected remotely sensed data is transmitted to the ground station through a low-power wireless communication channel. The multispectral data is then processed to provide useful information pertinent to the local terrain. Figure 1 shows the BalloonSat and samples of its wide-angle and telephoto visible imagery.

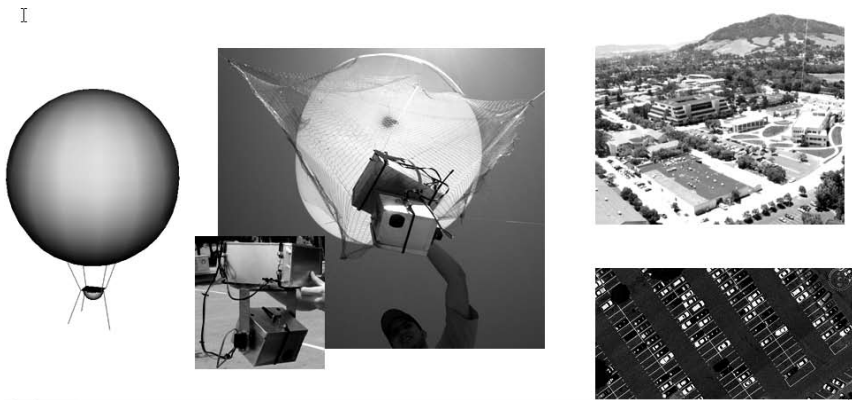


**Figure 1.** BalloonSat and samples of its wide-angle and telephoto visible imagery

The long term objective of this research is to develop digital image processing schemes to exploit the remotely sensed multispectral imagery collected by the BalloonSat in various applications useful for Cal Poly campus and the surrounding community. The current application being investigated is to provide a tool for the assessment of the status of the campus open parking lots. A robust image exploitation scheme to identify and count vehicles in a campus open parking lot has been successfully developed. New applications utilizing the recently added thermal imaging capability of BalloonSat will be developed in the near future.

## HARDWARE SYSTEM DESIGN: PAYLOAD

The various functions can be broken down into ground station and BalloonSat platform areas. Figure 2 shows the electrical, communication, and control systems for the BalloonSat. The ground station houses the Radio Control (R/C) transmitter for control of the pan, tilt, take picture, and reset servo commands. The commands are sent to the R/C receiver on the balloon that is connected to the microcontroller which interprets the signals and activates the servos appropriately. The digital, visible light camera stores its images on the SD memory card when the servo physically operates the shutter. At the same time, the thermal camera in the camera box outputs a live video stream. The thermal camera's video stream is transmitted in real time through a video transmitter in the upper box down to a video receiver at the base station, where it is displayed on a laptop via a TV tuner card. Operators use the images from the video feedback to aim the camera while the payload is aloft.

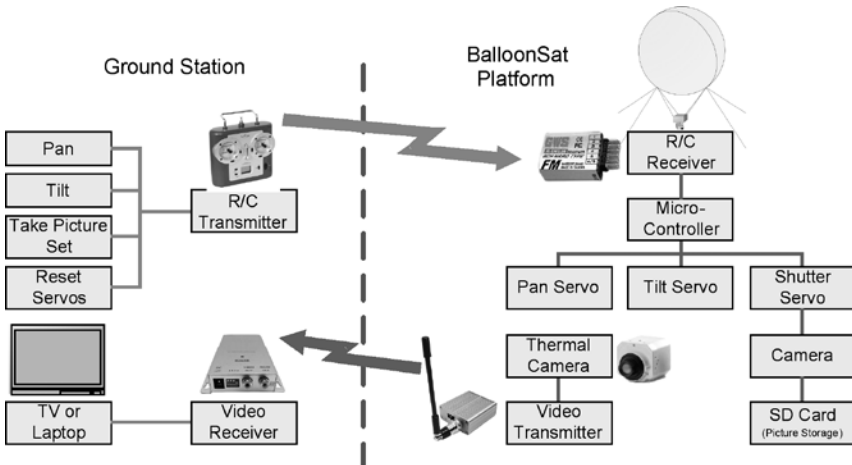


**Figure 2.** BalloonSat System Block Diagram

### Chassis Design

The chassis is designed to house the visible light camera, infrared (IR) lens and servo, and shutter release servo. The cameras have pan and tilt servos that have been designed and implemented specifically for this application. The dimensions of the lower housing were changed to allow for the added thermal camera and

the removal of the IR lens. The components are constructed from aluminum sheet stock.

### **Thermal Camera**

The new addition to the BalloonSat platform is a commercial thermal camera from FLIR Systems in Goleta, California. The camera has 320 by 240 pixel resolution and a 19mm lens. This compact camera has a cross section of two inches by two inches and weighs 155 grams. It has an uncooled core and a spectral response range of 8-14 micron. The added spectral information gathered by this compact and light weight camera will provide useful information that will more easily and efficiently accomplish project goals. While able to be remotely controlled via an RS-232 connection, the camera can also operate autonomously, outputting an analog video signal which is optimized for current light conditions. The camera operates at supply voltages from 5 to 24 Volts and dissipates an average of 1.6 Watts. It is also shock tolerant, capable of withstanding a 70-g shock pulse and operates near room temperature without requiring costly cooling system [1]. The analog video output of the thermal imager is a 320 by 240 pixel, NTFS encoding at 30 frames per second.

The high-resolution thermal images captured by this camera improve the ability to differentiate vehicles from the background due to their unique heat signatures. Unlike visible images, thermal images will be invariant to the type, color, or position of vehicles within the parking lot. Moreover, the surrounding blacktop and vegetation will also have distinct heat signatures. Hence, thermal images provided by this camera will significantly increase accuracy in the image processing as compared to when the platform was limited to visible and near-IR wavelengths.

### **Stability of the Balloon Rig**

Experience from previous launches raised several alarms about the stability and security of the weather balloon platform and its expensive payload. Previously, the payload was suspended from the balloon via netting over the balloon much like a hammock. This design did not provide adequate stability for the payload

during wind gusts. While the netting was lightweight, it increased the pressure exerted on the balloon where the net met with it (especially on the side opposite of the incident wind). The net was also prone to tangling and was very difficult to make even slight adjustments to its orientations during the launch process. To overcome these difficulties, the net was replaced with a rain fly, lowering pressure exerted on the balloon and securely holding the weather balloon in place under harsh flying conditions. The rain fly was not prone to tangling, did not contain any sharp cable ties, and was much easier to reposition during the launch process. As the weight of the rain fly and new tether system, which will be discussed shortly, was much increased, the diameter of the weather balloon and the amount of helium needed to be increased. Hence, a 13'x15'x7', 6 lb rain fly was purchased to accommodate the increased balloon diameter. Instead of suspending the payload, heavy-duty nylon strapping was sewn to the rain fly's straps and to straps looped through newly created holes through the upper housing's four corners. The integrity of the sewn connections provided a tensile strength, which far exceeded the requirements of this project (two people pulling in opposite directions could not sever the connection). Refer to Figure 3 below for the implemented rain fly system. Notice, the additional rope inserted around the horizontal circumference of the balloon, used to better contain the balloon while aloft.



**Figure 3.** Modified Balloon Rig

### **Electronics**

In order to organize the goals and capabilities of the electronics for the BalloonSat, a generalized block diagram for both the onboard and ground station electronics was created as seen in Figure 2. A controller board for the BalloonSat was designed and implemented. Figure 4 shows the controller board during construction. This board manages power and controls everything onboard the balloon. This circuit was designed to accomplish all the capabilities that were outlined in the system block diagrams. One important addition to the circuit was a 12 volt regulator that could be turned on and off from the microcontroller. This

regulator supplies power to the video transmitter, which happens to be somewhat of a power hog. The ability to turn this transmitter on and off gives us the option to go into a low power mode to conserve limited onboard power. After the schematic was built and tested physically on a breadboard, it was exported to a board layout. Some of the goals for the board design were to keep its size under two inches square, minimize the connections on the top side of the board, and to include component labeling on the top side of the board.

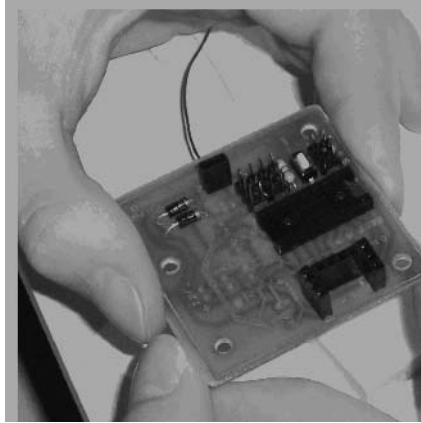


**Figure 4.** BalloonSat Controller Schematic

## SOFTWARE SYSTEM DESIGN -- DATA EXPLOITATION

The goal of the software research portion of the BalloonSat project is to develop image processing algorithms and techniques to extract physical features and information from the imagery taken aboard our aerial platform. Specifically, the main image processing goal is to develop a unique algorithm for extracting the number of parked vehicles from an aerial photograph of a parking lot. The eventual application would be to be able to launch a balloon platform satellite and collect parking lot populations automatically from images taken onboard the satellite.

With the addition of the thermal camera, the imaging capability of the BalloonSat now extends from the visible light (0.3 to 0.7 micron wavelengths) to the thermal range (8 to 14 microns wavelength). However, experimentation and

exploitation of the thermal imagery has just started and the final combined visible/thermal results will be presented in the future publications.

### **Automatic Vehicle Detection and Counting Problem**

Various methods have been used for vehicle extraction in several different kinds of applications using both visible and thermal imagery [1-8]. Many techniques involve using several different kinds of gray-level, color-level, or binary operations to create new images and then using a quantifiable metric to count the number of vehicles in the new image or images.

A human being would easily be able to discern the number of vehicles present in a picture of a parking lot, but writing algorithms that duplicate the visual and mental processes of a human is not a simple task. Computer software works in series of simple sequential tasks and enumerated quantities, so discerning a qualitative feature in a parking lot image involves many complex sequences of these simple tasks.

Nevertheless, there are many applications for algorithms like this one, which seek an automated way of extracting a useful feature from an image or set of images. Figure 5 illustrates some of the challenging issues to be considered relevant to identifying of cars in aerial photos of parking lots.

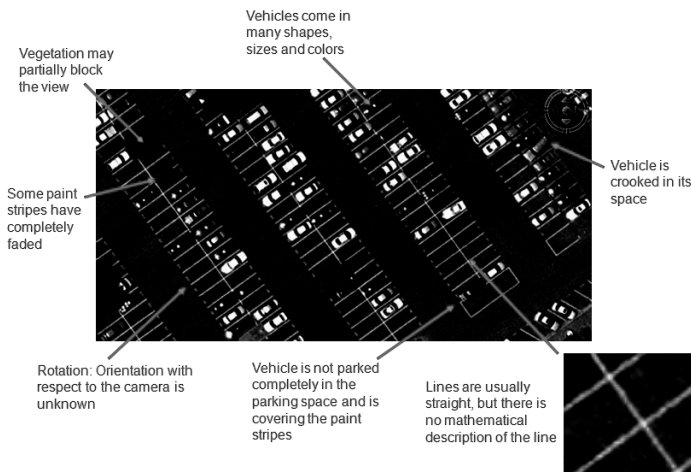


**Figure 5.** Challenges for the automatic vehicle detection and counting

There are two common approaches for this task, Blobbing and Correlation Raster. The blobbing concept involves taking a grayscale or Red-Green-Blue (RGB) image, such as a visible light parking lot input image, and converting it into a binary image, consisting of only 1s and 0s. Ideally, all of the pixels that were 1s in the binary image would be pixels that were part of a vehicle, and all of the 0s would be cement, dirt, trees, or some other type of terrain. Thus, the blobs could simply be counted to yield a vehicle count in the image.

The process of counting blobs is algorithmically quite easy and fast, and has been implemented in many programming languages, platforms and in numerous different kinds of applications. The challenge in any blobbing method is in creating the binary image. There are two basic schemes, Base Image Subtraction and Manual Blobbing, which are commonly used for counting blobs.

Base Image Subtraction is a method that would be difficult to implement given BalloonSat's platform. The idea is to collect a set of baseline images in which there are no vehicles in the parking lot, then take pictures later when the vehicles are present. With both images converted from RGB to grayscale, the baseline images can be subtracted from the populated images and the pixels that have a grayscale value near 0 can be removed with thresholding (setting any pixel that is within some set distance of 0 to 0). The remaining pixels can therefore be "blobbed", the blobs can be counted and output as a vehicle count.

The difficulty in Base Image Subtraction is due to the fact that the scale, size and position of the baseline images must be nearly identical to the images taken later. If done with a mounted, near-permanent or predictable aerial platform this might be possible to achieve, but with the unpredictability of the BalloonSat platform, this method is most likely unattainable.

Manual Blobbing involves using a single input image (populated with vehicles) which is processed and converted to a binary image and then blobbed. This method actually involves a series of other embedded methods in order to convert the input image to a binary image. The difficulty in this method is due to all of the issues outlined in Figure 5, and is exacerbated by the parking lot lines. The parking lot lines, even when the cars park properly, often end up intruding into

the binary image and blending multiple vehicle blobs into one another, yielding a very inaccurate vehicle count.

Other methods were attempted this year to filter out the parking lot lines for Manual Blobbing. The most successful involved using the Hough Transform to discover straight lines (parking lot lines) in the image and filtering out the pixels that contributed to these lines (or pixels that were very similar). The problem with this method is that a good amount of vehicle information was filtered out as well, including most white, gray, silver and light blue vehicles.

Correlation Raster is a vehicle count extraction method that uses a pre-extracted vehicle mask, a small image taken from another sample image which looked exactly like a vehicle. The mask is then run through the image in a Raster fashion (from the top-left to the bottom-right) and a discrete cross-correlation is calculated between the mask and the input image pixels it was placed upon. This correlation value is then plotted in a new image, which is filtered, based on a grayscale threshold, and the remaining pixel blobs are counted as vehicles. This method is quite slow, as it involved iterating through every single pixel in the input image and for each pixel, iterating again through all of the pixels located underneath the mask. This requires nearly  $n^3$  (three nested loops) operations for an  $n$  by  $n$  image, as the size of the mask is approximately  $n$  in our test image set. The other major drawback of this method was that its results are not very accurate. For one, in our tests it only accounted for vehicles that matched the shape and color of the selected mask. Additionally masks could be used, but this would involve another Raster run, and given the number of different vehicle shapes and colors that need to be considered, the algorithm would very quickly become extremely slow to run, and still not necessarily be accurate. In addition to only partially accounting for all vehicle types, the method is not at all scalable. If the input images taken were not taken at *exactly* the same size and scale as the pre-extracted vehicle mask, then the method would not work at all, or a new mask would have to be manually created (which defeats the purpose of automation).

## **Developed Vehicle Identification and Counting Scheme**

The new method was dubbed Percent-Fill Raster. In this approach, instead of using a Rastered vehicle mask, a parking lot space length and width are extracted from the input image and used to create an empty mask. This mask would be run through a binary form of the input image and if the number of pixels underneath the mask exceeded some percentage threshold of the size of the mask, a 1 would be plotted in an output image. The number of 1s in the output image then yielded a vehicle count. The difficulty, again, was in the accuracy of the creation of the binary image. However, because of the considerations of the Percent-Fill mask, it was no longer of great concern that the parking lot lines be successfully filtered out. In other words, the binary image did not have to have separate pixel blobs (as would be required by the blob counting methods outlined above). The *Percent-Fill Raster* algorithm steps are outlined below.

### **Step One: *Grayscale Transformation***

This step is a very basic image processing operation which consists of a color space transformation from RGB to Luma-Chrominance (Y'UV) color spaces. The input images had intensities describing the amount of light in the red, green and blue bands. These images are fed through a simple matrix transform into the Y'UV color space and the Y' component (intensity) is used as the output gray level intensity.

### **Step Two: *Cement/Asphalt Gray-Level Extraction***

The gray level of the cement/asphalt/ (empty parking lot space) is used as a threshold to distinguish the vehicle from the asphalt/cement background. Extracting the level is done in a very simple manner: using the statistical mode of *all* of the gray levels in the input grayscale image, e.g., the gray level histogram.

### **Step Three: *Filtration of Trees & Vegetation***

This step aims to set all pixels that correspond to trees and vegetation to the gray level of the cement (so they will be ignored later). This step yielded some

improvement in the accuracy of the algorithm, as tree areas tended to be counted as vehicles beforehand.

Tree and vegetation filtration process involves the following procedure:

1. Computation of “green content” images:

Two images are computed directly from the input RGB components, i.e., red, green, and blue, of the color image. The R, G, and B images are treated separately, and the two new “green content” images are computed by subtracting the B image from the G image and the R image from the G image.

2. Set all nonzero pixels in the “green content” images to 1 (forming a binary image by using a threshold of 0).

3. Compute Logical AND of the two “green content” images:

If a pixel is a 1 in *both* “green content” images, then it is a 1 in the Logical AND image, otherwise it is a 0.

4. For all pixels, if it is a 1 in the Logical AND image, then set it to the cement gray level in the input grayscale image and use that as the output image with trees filtered out.

The basic concept behind the four filtering steps is to extract which pixels are dominantly green and have almost *no* red and blue content. If all pixels that were highly green were filtered out, then pixels in green cars or certain blue cars would be filtered out as well. But computing the two subtraction “green content” images and then computing their Logical AND ensures that the filtered pixels have only green information. Figure 6 shows a sample input image after the trees have been replaced with the cement gray level and the rest of the image has been converted to grayscale.

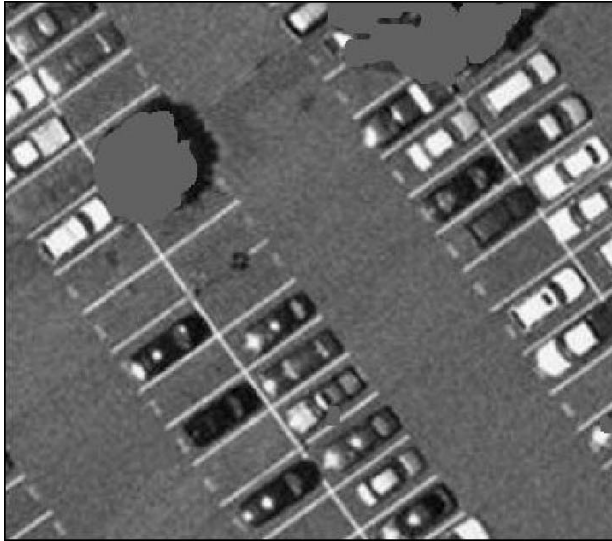


**Figure 6.** Grayscale Input After Filtration of Trees & Vegetation

#### **Step Four:** *Canny Edge Detection*

The goal of edge detection is to highlight pixels that are on the border or edge of a particular image region, such as the pixels on the edge of a vehicle next to parking lot cement. There are various gradient-based edge detectors including Prewitt, Sobel, and Laplacian, and Robert [9]. For this project, a non-mask Canny edge detector was used. Canny edge detection is a multi-stage edge detection algorithm based on Gaussian derivatives. The results of using Canny edge detection on the input grayscale images (after tree filtering) were quite successful compared to the results found with the classical Prewitt, Sobel, Laplacian and Roberts masks previously experimented with. These improved results also aided in the improved results of the next step, the Hough transform. A sample of an edge detected input image is shown in Figure 7. This image was taken after steps one through four were completed.



**Figure 7.** Sample Edge Detected Image

**Step Five:** *The Hough Transform*

The Hough Transform is used to find straight lines in images [10]. It is very powerful, especially in applications such as BalloonSat where it is known that straight lines will occur in the image, in this case the parking lot lines. The Hough Transform is a two-dimensional discrete transform (like the 2-D Discrete Fourier Transform or 2-D Discrete Cosine Transform) which transforms a binary image into what is called the Hough Space. The Hough Space is another two-dimensional matrix (or image) in which each pixel corresponds to a particular line that *could* be in the input image. If the level at some pixel in the Hough Space is high, or a maximum, then the line described by that pixel's location in the Hough Space probably exists in the input binary image as a series of 1s. A sample image was created in which the lines found in the Hough Space were overlaid on top of the input edge image in red to show which lines had been discovered. This image is shown in Figure 8.

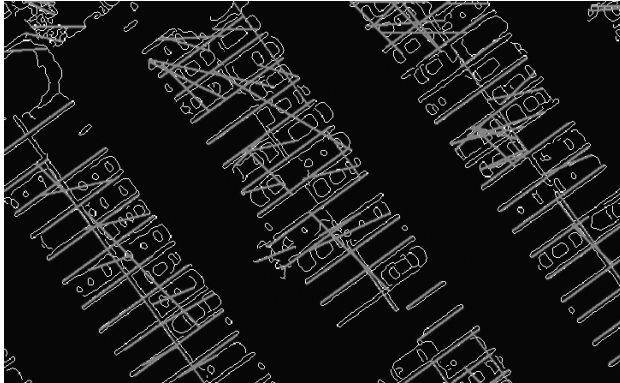


**Figure 8.** Sample Hough Transform Lines

**Step Six:** *Extraction of the Length & Width of the Mask, and the Angle of Rotation*

This step is unusual and important for the Percent-Fill Raster and image rotation steps. The goal is to take the returns from the Hough Transform and discern the length and width of a typical parking space, as well as the angle of rotation of the parking lot in the image. Since the results of the Hough Transform are obviously not perfect, this proves to be a difficult task.

To extract the angle of rotation, the statistical mode is again utilized on the Hough Space returns. The angle ( $\theta$ ) at which the most Hough Space maxima occur is the angle at which most of the lines are oriented. Since most of the lines returned by Hough are likely to be the parking lot lines, this angle will be the angle that the image needs to be rotated by to align it vertically.

This method produced very accurate results. The resulting lengths, widths, and angles of rotation were very consistently accurate for our test image set, and the length and width were only different from what a human could visually perceive (after zooming in) by 1 or 2 pixels at the most in each direction.

**Step Seven:** *Image Rotation*

The input grayscale image needs to be rotated so that the parking lot rows are aligned with the top and bottom of the image, and so that the Percent-Fill mask

can Raster through the image in a vertical alignment. Step six returned an angle that the image needed to be rotated by.

**Step Eight:** *Forming a Binary Image*

This step is actually a series of separate and unrelated simpler steps, some of which are commonly called morphological operations. If the method of vehicle counting were blobbing, then the separation of vehicle pixels from parking lot lines and other vehicles would be extremely crucial here. However, since blobbing is not the method used, this step has relaxed goals and characteristics, and occurs simply to separate out the parking lot cement (and effectively the trees) from the rest of the pixels. This leaves a binary image where all of the white pixels (1s) are either vehicles, parking lot lines, or some other unwanted disturbance. The resulting image is black and white, with the white pixels forming very large blobs made up of vehicles and parking lot lines. The next step in the algorithm will serve to differentiate which pixels contribute to vehicle space and which do not. A sample of the rotated binary image is shown in Figure 9.



**Figure 9.** Sample Rotated Binary Image

**Step Nine:** *Raster Percent-Fill Mask*

Step six provided an accurate measure of the length and width of a typical parking space, and the idea behind step nine is to find how often in the binary image (from step eight) the white pixels fill up that mask in the way that a vehicle would. If the mask is placed at some point in the binary image, and it is popu-

lated with a large majority of white pixels, chances are the mask is sitting on top of a vehicle.

Drawing this concept out, the mask is simply run through the image in a Raster pattern to form a new binary image that displays white pixels, i.e., “1” pixels, corresponding to the center of the mask locations for which the percentage of pixels underneath the mask exceeds some threshold. The threshold was empirically selected to be 70%. This step effectively serves to filter out the consideration of the parking lot lines. As can be seen in Figure 9, the parking lot lines contribute to a good portion of the white pixels in the image, but since they will not be enough to meet a large percent-fill threshold, they will be omitted from the Percent-Fill output image, and thus will not be considered in the output vehicle count. This can be seen in the sample Percent-Fill output image, shown in Figure 10.



**Figure 10.** Sample Percent-Fill Output Image

### **Step Ten:** *Counting the Vehicles*

The last step is extremely simple, being comprised of nothing more than a short calculation. All of the white pixels found in the Percent-fill output image are counted up (i.e. all of the pixels in the binary input from step eight that filled the mask to a percentage threshold). That count is then divided by the area of the mask (the extracted length multiplied by the width) and that value is printed out

as the count of vehicles in the original input image. Essentially, it is assumed that the number of pixels that are white in the Percent-Fill image is relatively equal to the number of pixels that were part of a vehicle in the original image. Thus, if you divide the number of white pixels by the size of a vehicle (in pixels), you will get a count of the vehicles that are in the original input image. Theoretically, this same operation could be performed on the binary image obtained in step eight, but that image has a large number of pixels that correspond to parking lot lines. Step nine is therefore required to remove the consideration of these pixels.

## EXPERIMENTAL RESULTS

The algorithm was tested on a sample set of 8 similar aerial parking lot photos taken from the BalloonSat. The algorithm did not do any pre-processing of the images, as the images were taken with a good camera and good lighting. Consequently, in order to process other image types, there might need to be additional front-end pre-processing, such as histogram equalization/specification or tone adjustment. The input test images were of varying size, scale and orientation. They were in RGB format and a sample is shown in Figure 11. The number of cars in each image was counted visually for comparison to the algorithm, and the results obtained from the algorithm's output are shown in Figure 12. The maximum percent difference between the actual count and the algorithm's output count is 12%, and the average percent difference for all eight images is 6.9%, which is considerably more accurate than previous BalloonSat results.

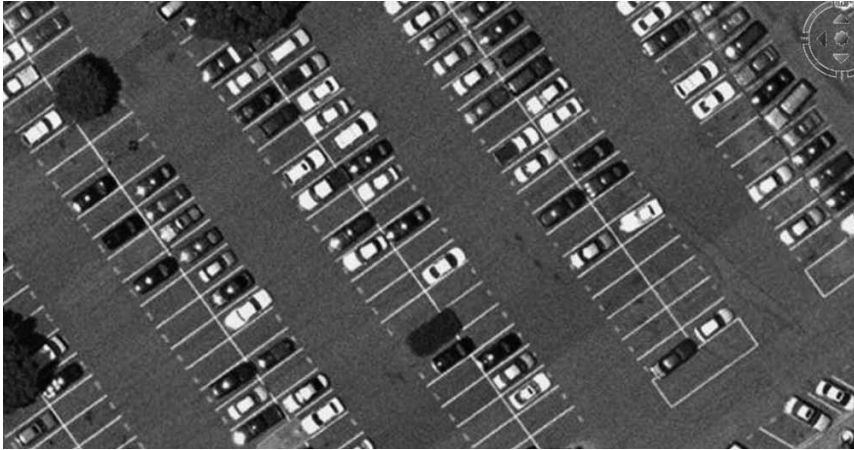


**Figure 11.** Input RGB Test Image

Test Image	Resolution	Vehicles in Image	Algorithm Output Count	% Difference
lot1.jpg	1035 x 524	80	80	0.00%
lot2.jpg	502 x 524	44	39	11.4%
lot3.jpg	332 x 524	25	23	8.00%
lot4.jpg	1035 x 352	60	58	3.33%
lot5.jpg	1035 x 206	20	20	0.00%
lot6.jpg	368 x 470	56	62	10.7%
lot7.jpg	524 x 332	25	22	12.0%
lot8.jpg	352 x 368	51	56	9.80%

**Figure 12.** Table of Image Processing Algorithm Results

## CONCLUSION

Students were successfully able to design, implement, and test a low-cost tethered helium-filled weather balloon remote sensing station. The onboard visible, infrared, and thermal sensors have wireless remote pan and zoom with real-time video monitoring capabilities. The collected remotely sensed data was transmitted to a ground station through a low-power wireless communication channel. Initial launches of the new and improved BalloonSat indicated more physical stability and wind-tolerance than previous designs. BalloonSat was successfully launched on Cal Poly campus. The collected multispectral data was exploited to provide

useful information pertinent to the local terrain including the assessment of the status of the campus open parking lots. A robust image exploitation scheme to identify and count vehicles in a campus open parking lot was successfully developed. In the near future, with the recently added thermal imaging capability, more challenging and multi-sensor exploitation schemes will be developed for such applications as campus security, campus traffic monitoring, and campus tours.

## WORKS CITED

- [1] Pyroelectric imaging, B.M. Kulwicki et al, Applications of Ferroelectrics, Proceedings of the Eighth IEEE International Symposium on, Proceedings of the Eighth IEEE International Symposium on, 1993
- [2] Methods of analyzing traffic imagery collected from aerial platforms, A. Angel et al., IEEE Transactions on Intelligent Transportation Systems. Vol. 4, Issue 2, pp 99-107, 2003
- [3] The Use of Photographic Methods for Traffic Data Collection, J. B. Garner, J et al. Uren, The Photogrammetric Record, vol. 7, Issue 41, pp 555-567, 2006
- [4] Car detection in aerial thermal images by local and global evidence accumulation, S. Hinz et al, Pattern Recognition Letters, vol. 27, Issue 4, 2006
- [5] Automatic Vehicle Detection in Satellite Images, J. Leitloff et al, International Archives of Photogrammetry, Remote Sensing, and Spatial Information Sciences, vol. 36, Issue 3, 2006.
- [6] Detection of Vehicles and Vehicle Queues for Road Monitoring Using High Resolution Aerial Images, S. Hinz, Proceedings of 9th World Multiconference on Systemics, Cybernetics and Informatics, July 2005
- [7] Fast and Subpixel Precise Blob Detection and Attribution, S.Hinz, Proceedings of ICIP 05, Sept. 2005
- [8] Estimation of vehicle movement in urban areas from thermal video sequences, E. Michaelsen et al, 2nd GRSS/ISPRS Joint Workshop on "Data Fusion and Remote Sensing over Urban Areas", 2003
- [9] Edge detection techniques - an overview, D. Ziou et al, International Journal of Pattern Recognition and Image Analysis, vol. 8, pp 537-559, 1998
- [10] A modified Hough transform for line detection and its performance, O. Chutatape et al, Pattern recognition, vol. 32, pp 181-192, 1999

# REPRODUCTIVE LIFE HISTORY AND THE EFFECTS OF SEX AND SEASON ON MORPHOLOGY IN *CROTALUS* *OREGANUS* (NORTHERN PACIFIC RATTLESNAKES)

Benjamin Kwittken, Student Author  
Dr. Emily N. Taylor, Research Advisor

## ABSTRACT

Over continuing long term data collection, two trends of reproductive ecology of a population of Northern Pacific Rattlesnakes (*Crotalus oreganus*) in the Carrizo Plain of central California have been discovered using radiotelemetry, snout-vent length and mass data. Using the co-occurrence of male and female snakes as a proxy for courtship, we have also discovered that the snakes mate in the spring and fall. Using snout-vent length and mass, male snakes are larger than female

snakes. The team has also begun to collect blood samples along with all of the other data for future analysis. We hope to use the blood samples collected to determine the effects of sex and season on immune function with methods such as flow cytometry.

## INTRODUCTION

Rattlesnakes are carnivorous ectothermic heterotherms like all snakes and most reptiles. Around fifty species exist in the Americas today. Their name is derived from the rattle located at the tip of their tails. The rattle is used as a warning device when the snakes feel threatened. The scientific name *Crotalus* is derived from the Greek word for “castanet”.

Some species of rattlesnakes mate only once per year (spring or fall), while others mate at both times (Beaupre et al.,1998), (Duvall 1998). All species are viviparous and young are self-sufficient from birth (Klauber, 1997).

Dr. Emily N. Taylor began researching the Northern Pacific Rattlesnake, *Crotalus oreganus*, at Cal Poly San Luis Obispo where she is a biology professor. In the fall of the 2006, Taylor began researching a rattlesnake population in the Chimineas Ranch in the Carrizo Plain of California. The ranch is located about 60 miles east of Cal Poly.

*Crotalus oreganus* is the only species of rattlesnake to inhabit the Carrizo Plain. Taylor hopes to better understand reproductive behaviors of this species. Reproductive activity is to be studied extensively. It is hypothesized that the majority of the snakes’ movements and location choices during breeding seasons are dependent on optimal breeding conditions.

Because Taylor’s research concerns population trends, much time is needed to collect data. The data to be further augmented are seasonal snake location changes and qualitative data from observation of behavior and reproductive interaction. I intend to switch my focus from initially collecting data in the field to analyzing leukocytes from blood sample obtained in the field by other team members with flow cytometry. The project is a work in progress.

## BACKGROUND

Many species exhibit sexual dimorphism: phenotypic differences between sexes. Most snake species, including rattlesnakes, exhibit size dimorphism. Size dimorphism has been documented in Western Diamond-Backed Rattlesnakes (*Crotalus atrox*). Adult male snakes were larger in size than adult females (Beaupre et al., 1998). The efficacy of increased male size may be in reproductive success (Brown, 2000). Until now, size dimorphism has not been studied in *C. oreganus*.

*Crotalus oreganus* populations in Idaho have been found to mate biannually; in fall and spring (Diller and Wallace, 2002). Reproduction occurs biennially; every other year. Females usually skip years because it takes a while to gain enough fat to support a litter. The same temporal trend in reproduction appears to prevail in *C. oreganus* populations in the Carrizo Plain.

Because little is known about *C. oreganus*, more research must be conducted to determine the role the species plays in the ecosystem. Before we can understand this role, it is necessary to characterize intra-specific interactions.

## METHODS

In the fall through spring of 2006-07, radio transmitters were surgically inserted (see Figure 1) into the abdomens of 20 snakes (10 male and 10 female) in order to gain data regarding their movements. The sexes of the snakes were noted during their original capture. The snout-vent lengths and masses of each snake were also recorded. Snakes were assigned numbers (1-20) with different radio frequencies. The snakes were placed at the exact locations of their original capture. All of the snakes are within the close range of one another (approximately 0.25 miles). Location data are collected weekly during the active months of spring through early fall. Location data are collected using a radiotelemetry receiver and antenna (Figure 2). Once the data collector locates the snake, a description of the behavior of the snake if it is visible and a qualitative description of the snake's location are recorded. Quantitative data concerning the snake's location are noted as well using a Global Positioning Device (GPS). Latitude, longitude and elevation are gained from the GPS. Beginning Spring Quarter 2008, monthly blood samples

were collected (Figure 3), and blood smears were made to obtain immunological data (Figure 4).



**Figure 1.** Surgical procedure for radio transmitter implantation.



**Figure 2.** The author using radiotelemetry to locate snakes.



**Figure 3.** Blood is collected from the snake for lab analysis.

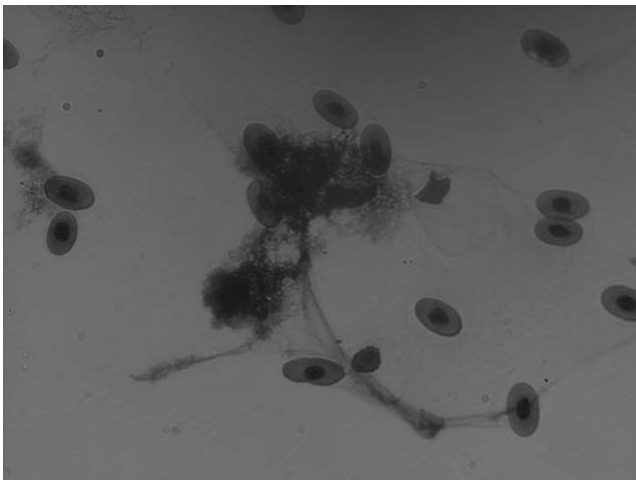


**Figure 4.** Blood smears are made with parts of the blood samples collected in the field.

All snake handling is done by the experienced professors and graduate stu-

dents for safety reasons. After snakes to be captured are located, tongs are used to hold the snake in one place while a clear plastic tube is placed over the snake from the head end. Once this process is completed, the capturer holds the snakes body and tube with one hand and the caudal portion of the snake with the other for data collection (Figure 5). A blood sample is collected intravenously via the caudal vein on the ventral side of the snake just superior to the rattle (Figure 3). The snout-vent length is then measured and after the snake is weighed in a bag. The rattlesnake is promptly and cautiously released by holding the bag with the opening side down.



**Figure 5.** A rattlesnake is "tubed" for safe administration of anesthesia and data collection

I will be using flow cytometry of the Animal Science Department to analyze the blood cells. Flow cytometry is one of the cutting edge technologies for biological analysis of small organisms such as bacteria or cells. With this technology I will be able to quantify various aspects of the snake blood cells that I would not be able to do with a microscope alone. I am hoping to search for the presence of particular identifying cell receptors. I will specifically be looking for immune cell receptors. Once this task is complete, I will be able to observe seasonal and sexual differences in immune function.

## RESULTS AND DISCUSSION

I went to the study site to collect data twice during the 2008 Winter Quarter. The snakes are known to hibernate during the winter, therefore none were seen in the open until a survey during the beginning of March. Each data collection took roughly one day. At times of great activity such as March 8 through March 9,

data were collected twice (e.g., on a Saturday and Sunday). Data collection takes a great amount of time because each snake needs to be located and time is necessary to travel to the site. Also, the number of snakes is continuously climbing.

One of the snakes was killed and consumed by a predator. This was determined because the radio transmitter was found on the ground covered in tooth marks and the most probable way for this to occur would be the natural predation of the snake. A new snake will need to have a radio transmitter implanted in place of the lost snake. The vast majority of the snakes were underground. Again this relatively inactive behavior can be accounted for by the weather conditions.

From data collected throughout the study, size dimorphism is apparent in *C. oregonus*. Males have a greater snout-vent length than females. Because the two-tailed P value was less than 0.001, the difference is statistically significant (Figure 6). The males are also more massive than females. Again the difference is statistically significant with the two-tailed P value less than 0.001 (Figure 7).

Because copulation events are difficult to observe, males found with females was used as a proxy for reproduction events. This is an accepted practice in herpetology because rattlesnakes are otherwise solitary and male-female consortships tend to occur only in the breeding seasons. From the data collected over that past year, mating in *C. oregonus* seems to be biannual, occurring in the fall months and more so in spring (Figure 8). This mating season allows for breeding to be more flexible in Northern Pacific Rattlesnakes than other species which only have one reproductive period each year. A Northern Pacific Rattlesnake female may mate with a male in the fall, store his sperm through the winter and mate with another male (or more) in the spring. Then when she ovulates in late spring her clutch could be fathered by multiple males. This fertilization by multiple males offers a greater chance that more offspring will survive and also lends itself to more variation in the gene pool. It also allows females to offer their young the best chance for survival. If a female were forced to give birth at the same time every year, she may be forced to place her newborn offspring in an unfavorable environment. With the spring/fall choice, the female is able to censor the environment of her offspring.

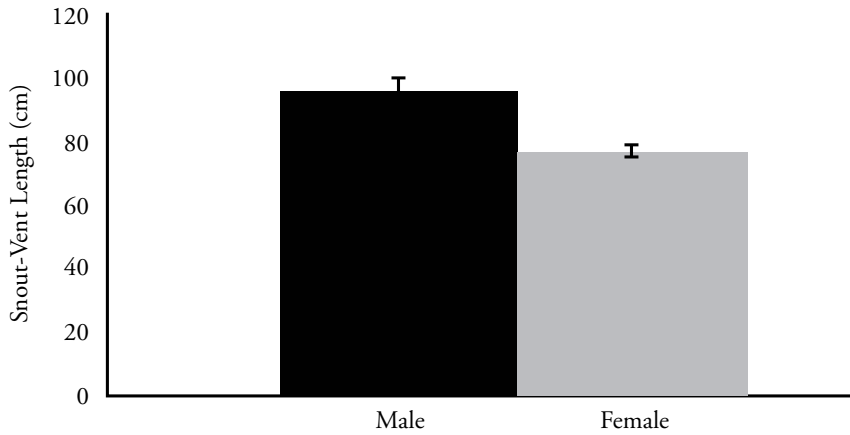


**Figure 6.** The lengths from snout to vent (cloacae) were measured and averaged for ten male and ten female *C. oregonus*. Males are significantly longer than females ( $p < 0.001$ ).

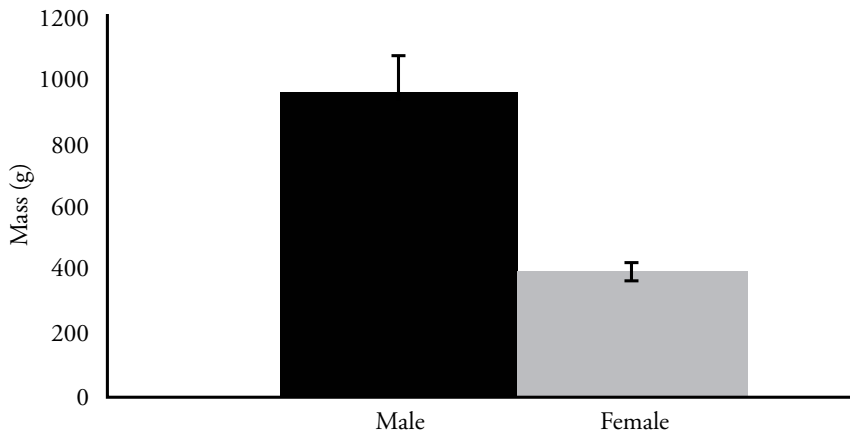


**Figure 7.** The masses were measured and averaged for ten male and ten female *C. oregonus*. Males are significantly more massive than females ( $p < 0.001$ ).

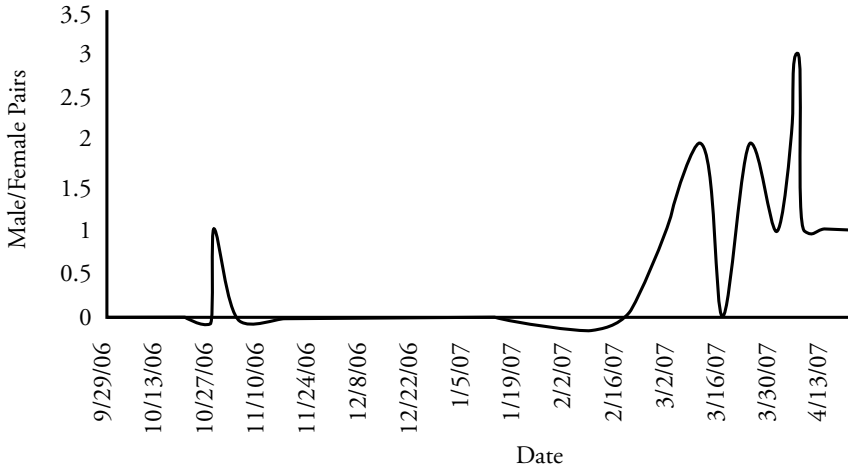


**Figure 8.** On each date of observation from September 29, 2006 to May 24, 2007 the number of male female pairs observed is recorded.

## CONCLUSIONS

Radiotelemetry has been and will continue to be used to collect data regarding reproductive behavior and movements of *C. oreganus*. Sexual dimorphism has been found to occur; males are larger than females in snout-vent length and mass. There is little data collection during the winter because the snakes are in hibernation. Data collection commences each spring when the snakes are most active.

I have mastered the radiotelemetry technique, use of global positioning systems (GPS). I am looking forward to moving the research forward with the use of flow cytometry. I would recommend this research to anyone who enjoys adventure and unique taboo fauna.

## ACKNOWLEDGEMENTS

I would like to thank Emily Taylor for allowing me to learn about her research and patiently putting up with my naïve herpetological melodrama. I would like to thank Marty Felder for teaching me about reptiles and life. I would like to thank Craig Lind and Peter Jackson-Tooby for sharing the experience of learning

with me and informing me about how the research experience works. I would like to thank the California Department of Fish and Game of California for allowing us access to Chimineas Ranch to conduct our research.

## WORKS CITED

- Beaupre, S. J., D. Duvall, J. O'Leile. Ontogenetic Variation in Growth and Sexual Size Dimorphism in a Central Arizona Population of the Western Diamondback Rattlesnake (*Crotalus atrox*). Copeia 1(1998): 40-47.
- Brown, G. P..Thermal Ecology and Sexual Size Dimorphism in Northern Water Snakes, *Nerodia sipedon*. Ecological Monographs 70(2000): 311.
- Diller, L.V., R. L. Wallace. Growth, Reproduction, and Survival In a Population Of *Crotalus viridis oregonus* In North Central Idaho. Herpetological Monographs 16 (2002): 26-45.
- Duvall, D.. Sexual Strategy and Size Dimorphism in Rattlesnakes. American Zoologist 38(1998): 152.
- Klauber, L. M.. Rattlesnakes: Their Habits, Life Histories, and Influence on Mankind. New Scientist 1-2(1997): 56.

# SIMULATIONS OF THE POLARIZATION DEPENDENCE OF THE LIGHT POTENTIAL EQUATION IN QUANTUM COMPUTING

Bert David Copsey, Student Author  
Dr. Katharina Gillen, Research Advisor

## ABSTRACT

Many methods of quantum computing are currently being researched because quantum computers may be able to perform certain calculations that we currently cannot because they would take the age of the universe. To create a viable quantum computer one must be able to create a multiple qubit gate. For our specific approach, neutral atom quantum computing, one must find a way to bring two atoms together, entangle them and separate them in order to create a multiple qubit gate. In our research we explored a way of facilitating the creation of a multiple qubit gate using the diffraction pattern created by two polarized lasers incident upon a

pinhole. We found that it may be possible to create moveable atom traps using this approach and thus it may be possible to create multiple qubit gates using this approach.

## INTRODUCTION

Quantum computing is being researched because in theory quantum computers can perform certain calculations much faster than a conventional computer. While a conventional computer's most basic components are bits, a quantum computer's most basic components are quantum mechanical bits also known as qubits. Quantum mechanical bits can be made from any quantum mechanical particle, such as atoms, electrons and photons. The big difference between a qubit and a classical bit is that while a bit can be either one or zero at any given time a qubit can be both one and zero at the same time. This property of qubits would allow us to store much more information on them than on a conventional bit which could lead to much faster computations of certain calculations.

Many methods of quantum computing are currently being researched. Some involve trapping quantum mechanical particles in solids and others involve trapping quantum mechanical particles using light [1]. There are advantages and disadvantages to all of the various methods being researched. Some, like three dimensional optical lattices have scalability, meaning that many qubits can be created and held together, but lack things like addressability and the ability to create multiple qubit gates [2]. In order to create a viable quantum computer all of these are necessary [3]. One must have scalability, addressability, and be able to create multiple qubit gates. Addressability is the ability to interact with an individual bit and is required in order to initiate calculations and read out of said calculation as well as implement gates. Scalability is necessary to attain a system with enough qubits in order to perform larger scale calculations. Multiple qubit gates are required in order to perform calculations that require multiple inputs and outputs. While multiple qubit gates have been created using nuclear magnetic resonance methods; this method currently lacks the scalability to perform larger scale calculations.

The specific approach we are exploring uses a few key properties of quantum mechanical particles and the effects of light polarization. The most mysterious of quantum effects that this approach exploits is entanglement. Entanglement is the linking of quantum mechanical particles through interaction. Two atoms that have been entangled can be separated a distance as large as the universe and yet what happens to one instantly happens to the other on the other side of the universe. Entanglement is required to create a viable quantum computer because without entanglement it would be impossible to link two quantum mechanical particles and thus impossible to create a multiple qubit gate.

The second key property of quantum mechanical particles that we exploit is superposition. Quantum mechanical particles can be in a combination of internal states at the same time. Superposition is the idea that these states can be combined to form an overall state that can be normalized to one. As applied to quantum computing this means that the total internal state of a qubit can be broken into two parts that can be used to represent the two states of a quantum computer. A few examples of how this is mathematically possible are shown in Figure 1.

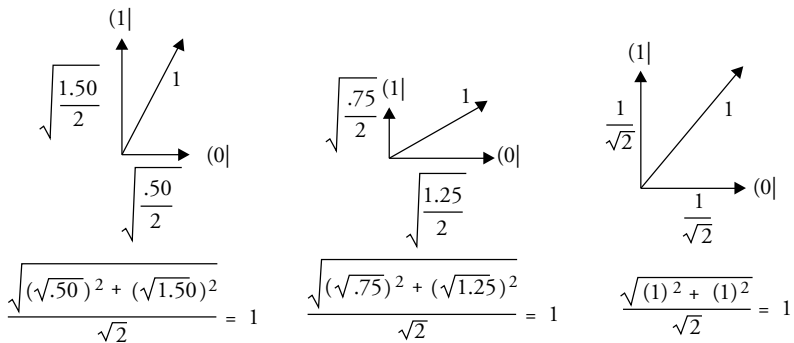


**Figure 1.** A simple example of how superposition works in which all vectors are normalized to 1.

The final physical property we are trying to exploit is light polarization. Light can propagate in a number of ways. Light can be linearly polarized, circularly polarized, elliptically polarized or a mixture thereof. Linearly polarized

light propagates in such a way that if you were to look at the line traced out by the electric field vector it would appear to form a straight line. As circularly polarized light propagates the electric field vector appears to trace a circle. This is because as the electric field vector is composed of two electric fields that are exactly 90 degrees out of phase and have the same magnitude. Elliptically polarized light is created in two ways. One way is similar to the way circularly polarized light is created. There are two electric field vectors that are exactly 90 degrees out of phase; however, the two electric fields are not the same magnitude. This results in the overall electric field vector appearing to rotate and change length such that the overall electric field vector appears to trace out an ellipse. Another way that elliptically polarized light can be created is if the electric field vectors are anything but 90 degrees out of phase, regardless of their magnitude. This results in the overall vector tracing out an elliptical pattern. These types of polarizations are shown in Figure 2. [4].

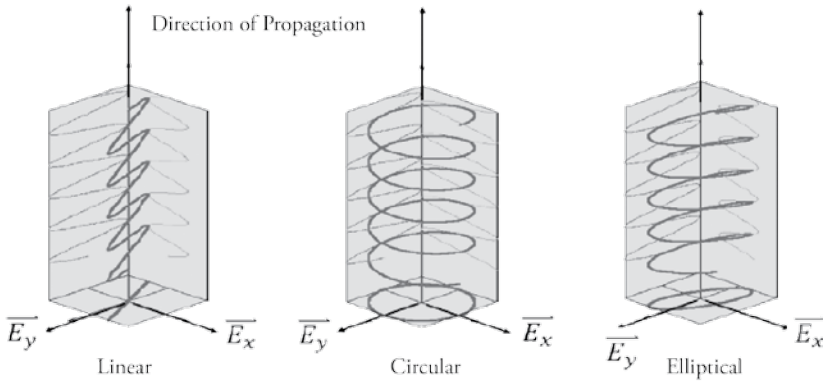


**Figure 2.** Examples of how the various polarizations of light propagate [4].

In this project, we are exploring the possibility of facilitating multiple qubit gates using a method similar to the three-dimensional optical traps mentioned earlier [2]. Currently, we are exploring the possibility of creating three dimensional optical traps using lasers that are incident on a pinhole. When lasers are incident upon a pin hole they create diffraction on the other side of the pinhole. An example of this diffraction pattern is shown in Figure 3 [5].

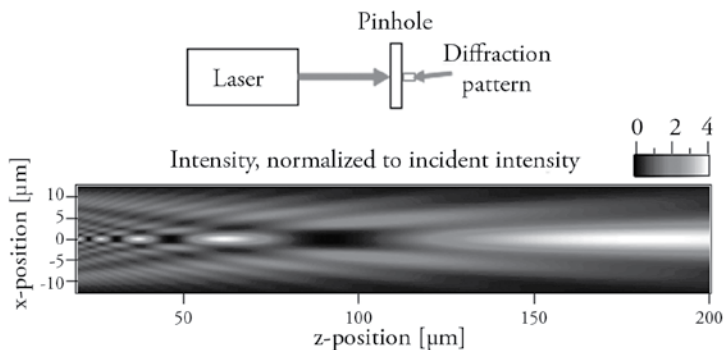


**Figure 3.** The diffraction pattern created by light incident on an aperture [5].

We are exploring the possibility of creating two different traps in the same intensity pattern using lasers of different polarization that are going through the same pinhole (see Figure 4). This looks very similar to the above trap; however, it has two dark spots instead of one. Since atoms can be in polarization sensitive states it may be possible to create two traps that contain atoms of different internal states that can be moved using the angle between the two lasers. One problem that arises when bringing traps together is that contents of each trap can move from one trap to the other. In this approach, this is not a concern because the atoms are in polarization sensitive states and are trapped using polarized light. This means that if two traps were brought together, the contents of each trap would not go into the other because they are only sensitive to the trap created by one specific polarization of light.

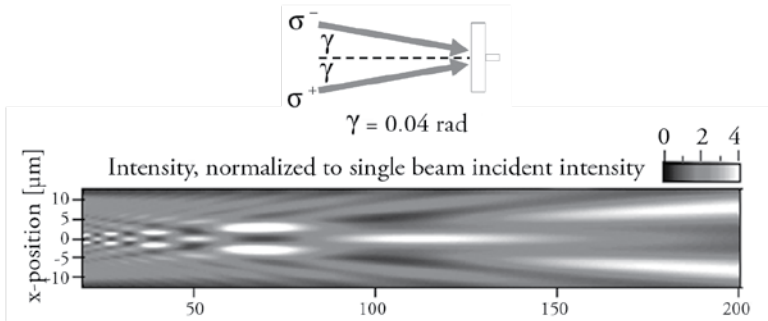


**Figure 4.** Diffraction pattern created by two lasers of different polarization incident on a pinhole

## THEORY

We began with the compact form of the light potential equation shown in Figure 5. First we derived the explicit form of the light potential equation (shown in Figure 6) and then programmed it into Mathematica so that we could use the program to simulate various optical traps.

$$\begin{array}{c}
 \boxed{\text{Polarization Tensor}} \\
 \downarrow \\
 \hat{U}(\mathbf{x}) = -\mathbf{E}_L^*(\mathbf{x}) \cdot \hat{\alpha} \cdot \mathbf{E}_L(\mathbf{x}) \\
 \uparrow \qquad \qquad \qquad \uparrow \\
 \boxed{\text{Electric Field Terms}}
 \end{array}$$

**Figure 5.** The compact form the light potential equation [6].

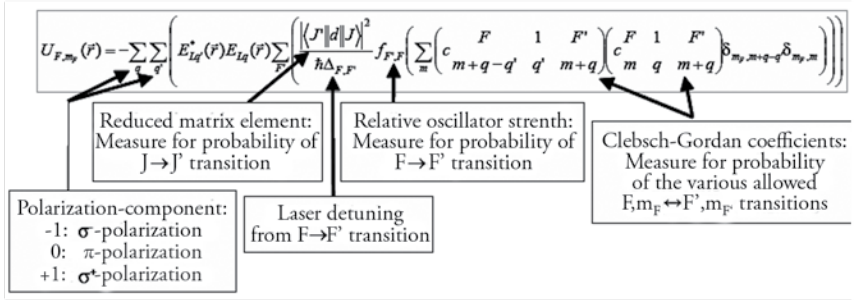


**Figure 6.** The explicit form the light potential equation and explanations of terms [6, 7].

## METHODS

We programmed the explicit form the light potential equation into Mathematica in order to solve the light potential equation much more easily. Using this program we can generate simulations much more quickly and spend more of our time coming up with light traps that we can simulate. After performing our test case, we had to modify the code to accept the electric fields as a table of information rather than a mathematical function. This is because we received the electric field data as a list of data from Dr. Glen Gillen rather than representing the electric fields as functions. We chose to model the fields this way because the diffraction pattern is very complex and cannot be represented as a function. Using our code and the electric field data we were able to calculate the trapping potential of the diffraction pattern due to the pin-hole for several incident laser beam angles.

## RESULTS

During this quarter we further developed the code required to simulate the trapping potentials of very complex light patterns such as diffraction patterns. Using this code we were able to simulate the trapping potential of the diffraction pattern created when one left-circularly polarized laser ( $\sigma_-$ ) and one right-circularly polarized laser ( $\sigma_+$ ) are incident upon the same pin-hole. Our overall goal was to

investigate the possibility of trapping and manipulating the locations of two different atoms in the same intensity pattern using the polarization dependence of optical traps. Figures 7 and 8 show the intensity patterns as well as the trapping potentials seen by each atom, one in  $m_F = +1$  and one in  $m_F = -1$ , of two differently polarized lasers incident upon a pinhole. Figure 7 shows the trapping potential for a small angle between the two lasers ( $\gamma=0.02$  radians) and Figure 8 shows the trapping potential for a large angle between the two lasers.

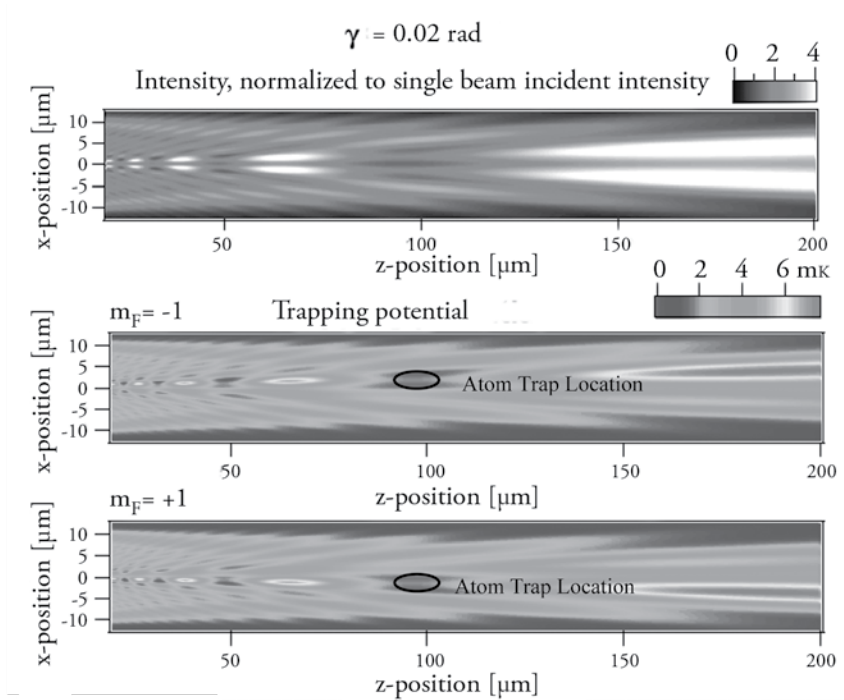


**Figure 7.** The intensity pattern and trapping potentials for a small angle ( $\gamma=0.02$  radians) between the two lasers.

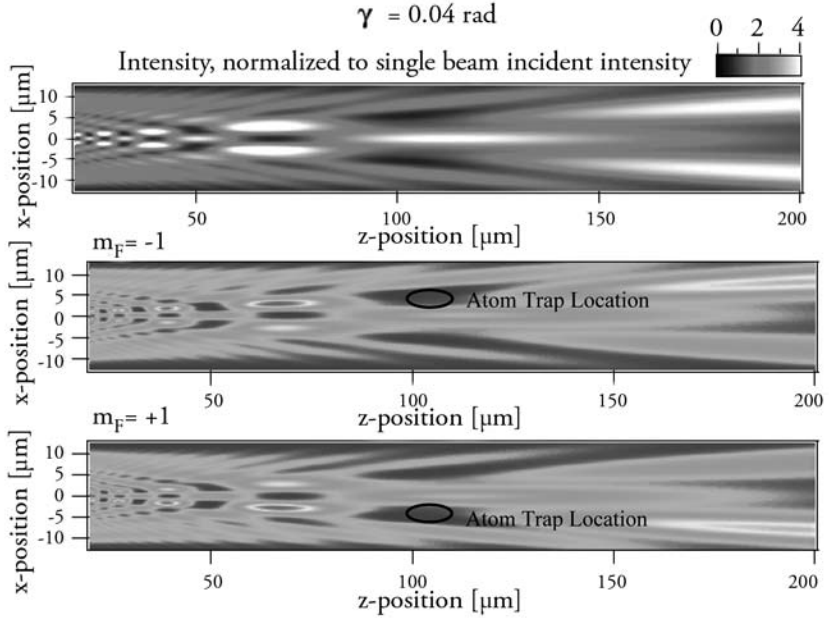


**Figure 8.** The intensity pattern and trapping potentials for a large angle ( $\gamma = 0.04$  radians) between the two lasers.

The two trapping potential diagrams shown under each intensity pattern can be thought of as being right on top of each other. The larger dark blue spots are where we are planning on trapping atoms. For the diagram of the smaller angle the two traps are very close together. This means that the two can be brought very close together without the atoms jumping from one trap to the other. In Figure 8 the traps are starting to get relatively far apart. This means that the two traps can be brought together and apart by changing the angle between the two lasers being used to create the trap, which in turn means that the two atoms can be brought together, be entangled and then separated creating a two qubit gate.

## CONCLUSION

It may be possible to create light traps that can be used to manipulate the location of atoms using the diffraction pattern created by two differently polarized

lasers incident upon a pinhole. Using this approach it may be possible to create a multiple qubit gate using neutral atoms, the holy grail of neutral atom quantum computing.

We recently presented these findings at the annual meeting of the Division of Atomic, Molecular and Optical Physics at Pennsylvania State University. Our findings were well received among the scientific community and the simplicity of the approach was liked by all. Currently our future plans consist of setting up a lab in which to experimentally test the feasibility of this approach in practice.

## WORKS CITED

- [1] R.Grimm et al. "Optical dipole traps for neutral atoms" *Adv. AMO Phys.*, 42 (2000), 95-170
- [2] I. H. Deutsch et al. "Quantum Computing with Neutral Atoms in an Optical Lattice" *Fortschr. Phys.* 48 (2000) 9-11, 925-943
- [3] D. P. DiVincenzo, "The Physical Implementation of Quantum Computation" *Fortschr. Phys.* 48 (2000) 9-11, 771-783
- [4] "Polarization Diagram." 18 May 2008. Online image. Wikipedia. 1 June 2008. <<http://en.wikipedia.org/wiki/Polarization>>.
- [5] G. D. Gillen, et al. "Optical dipole traps for cold atoms using diffracted laser light" *Physical Review A* 73 (2006), 013409
- [6] I.Deutsch et al. "Quantum-state control in optical lattices" *Phys. Rev. A*, 57 3 (1998), 1972-1986
- [7] M. Tinkham, "Group Theory and Quantum Mechanics", 1964

# RAPID DETECTION OF TOTAL AND PATHOGENIC *VIBRIO* *PARAHAEMOLYTICUS* USING REAL-TIME PCR WITH TAQMAN® FLUORESCENT PROBES

Evan Markegard, Student Author  
Marie Yeung, Research Advisor

## ABSTRACT

*Vibrio parahaemolyticus* is found throughout the marine environment and is a major cause of foodborne illness around the world. Foodborne illnesses due to *V. parahaemolyticus* infections frequently trace back to the consumption of raw or undercooked seafood. The ability to detect *V. parahaemolyticus* in a rapid, sensitive, and specific manner is important to safeguard our food supply and prevent consumption of tainted shellfish. The objective of this study was to optimize a

detection assay for *V. parahaemolyticus*, with a focus on the pathogenic strains, based on real-time polymerase chain reaction (PCR) technology using pure cultures. Primers and TaqMan<sup>®</sup> fluorescent probes were custom designed to anneal to both the species specific thermolabile hemolysin (*tlh*) gene and the virulence marker thermostable direct hemolysin (*tdh*) gene to detect for the presence of total and pathogenic *V. parahaemolyticus* strains, respectively. Different strains ( $n=14$ ) of *V. parahaemolyticus* and other *Vibrio* species were tested in the real-time PCR assay. Conventional PCR results obtained in a previous study were used as the basis of comparison for determining sensitivity and specificity. The detection of *tlh* had 100% sensitivity (12/12) and specificity (2/2), whereas the *tdh* gene had 100% sensitivity (6/6) and 88% specificity (7/8). In addition, a standard curve using threshold cycle ( $C_T$ ) values was constructed for both genes and had  $R_2$  values of 0.98 and 0.99 for *tlh* and *tdh*, respectively. The limit of detection was 9.16 pg (for *tlh*) and 6.13 pg (for *tdh*) of purified *V. parahaemolyticus* DNA, corresponding to  $2.2 \times 10^3$  and  $1.5 \times 10^3$  cfu/ml, respectively. A rapid molecular detection method using real-time PCR was successfully developed and optimized for the detection of *tlh* and *tdh* in *V. parahaemolyticus*.

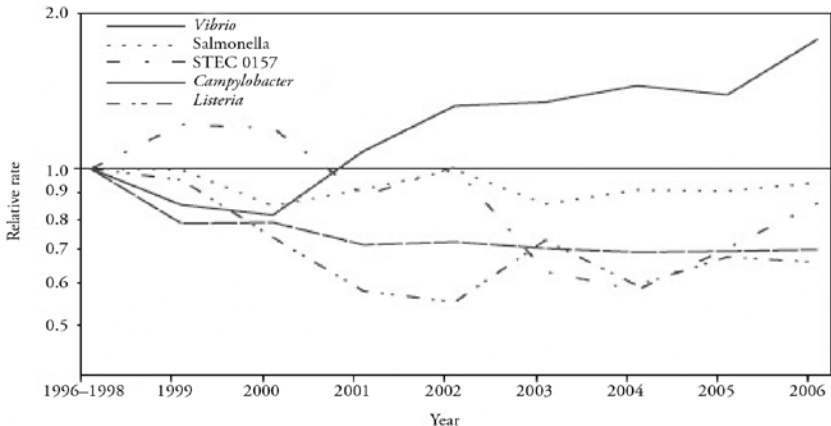
## INTRODUCTION

*Vibrio parahaemolyticus* is a gram-negative bacterium commonly found in estuarine and temperate coastal marine waters throughout the world (Ward and Bej, 2006). The organism can be found both free living or as commensals with reservoir hosts including fish and shellfish (Ward and Bej, 2006). Humans are susceptible hosts who can be infected through the consumption of raw or undercooked shellfish, particularly oysters (Yeung and Boor, 2004). Coastal countries have a greater risk of infection and outbreaks have occurred in North America, Southeast Asia, Japan, Russia, Spain, Taiwan and India (Ward and Bej, 2006). Outbreaks in the United States have occurred in the Pacific Northwest, Gulf, and Atlantic coastal regions.

*V. parahaemolyticus* is often associated with seafood-borne illnesses. Within 48 hours of ingesting the pathogenic strains, gastroenteritis symptoms appear

which include hyper secretion, gastroenteritis, nausea, vomiting, chills, fever, watery diarrhea, and sometimes abdominal cramping (Yeung and Boor, 2004). Gastroenteritis caused by *V. parahaemolyticus* is a self-limiting infection and most infected patients will recover without treatment (ProMed-mail 2007). In more severe cases, however, fluid replacement therapy or antibiotics such as tetracycline or doxycycline may be administered to shorten recovery time (Park et al., 2004). The mortality rate is approximately 1% (Yeung and Boor, 2004).

Cooking seafood properly could drastically reduce the risk of contracting the *V. parahaemolyticus* infections as they are sensitive to heat treatment (ProMED-mail 2007). Nevertheless, the increasing popularity of consuming raw or undercooked oysters, coupled with warmer global water temperatures that are induce for the growth of *V. parahaemolyticus*, have partly led to the re-emergence of this food pathogen (Figure 1) (CDC 2007).



\* Shiga toxin-producing *Escherichia coli*.

**Figure 1.** Among common foodborne pathogens in the United States, incidence of *Vibrio* (mostly *V. parahaemolyticus*) associated infection shows an upward trend (reprint from CDC 2007). The relative ratio is determined using the average number of illnesses in 1996-1998 as the denominator.

Ultimately, to prevent *V. parahaemolyticus* infections, harvested oysters should be screened for the presence of *V. parahaemolyticus* strains, particularly for those that have a pathogenic potential, prior to reaching the market place.

To this end, the objective of this study was to optimize a detection assay for *V. parahaemolyticus*, with a focus on the pathogenic strains, based on real-time polymerase chain reaction (PCR) technology using pure cultures.

## MATERIALS AND METHODS

To adopt real-time PCR, primers and probes were essential. New primers and TaqMan® fluorescent probes were designed to detect for the presence of *tlh* (indicative of non-pathogenic and pathogenic *V. parahaemolyticus*) and *tdh* (indicative of pathogenic strains) using Primer Express 2.0 and PrimerQuest. The sequence and other relevant properties are shown in Table 1. BLAST homology search against the NCBI GenBank database was done to verify the specificity of primers and probes. Primers and probes were supplied from Applied Biosystems Inc (Foster City, CA). DNA of *Vibrio* strains was extracted using a Qiagen Gram Negative Bacteria Purification Kit (Qiagen Inc, Valencia, CA). DNA was quantified using Qubit Quanti-iT DNA Broad Range Kit (Invitrogen Corp, Carlsbad, CA) and confirmed using Quant-iT PicoGreen dsDNA Kit (Invitrogen Corp). Final primer and probe concentrations were 0.4 µM and 0.2 µM respectively. All assays included a negative control made up of all reagents except template DNA was replaced with PCR grade H<sub>2</sub>O.

An Applied Biosystems Real-Time PCR 7300 System was used. The cycling program consisted a 15 s denature step at 95°C, 20 s annealing step at 57°C (*tdh*) or 58°C (*tlh*), and a 30 s extension step at 60°C. After 35 cycles, threshold cycle values were determined according to the build-in computer software program. Standard curves were constructed by first quantifying DNA template constituting DNA extracts of cell suspension of *V. parahaemolyticus* FSL-Y1-005 and FSL-Y1-013, then conducting real-time PCR on 10-fold serial dilutions of these extracts. The bacterial cell number in the cell suspension was also determined concurrently by standard plate count on tryptic soy agar supplemented with 2% NaCl.

**Table 1.** Real-Time PCR primer and probe target sets for the *tlh* and *tdh* genes. Each set was custom designed using consensus sequences from NCBI BLAST and Primer Express 2.0. The melting temperature, GC content, length, and specific fluorescent dyes and quenchers were all considered when designing the primers and probes.

Target Gene	Oligo-nucleotide	Sequence (5'-3')	T <sub>m</sub> (°C)	% GC	Length (nt)	Dye/Quencher
<i>tlh</i>	Forward Primer	AAAGCGGATTATGCA-GAAGCACTG	63	46	24	
	Reverse Primer	CGATCTCTTCTTGTGTT-GAGTACTTAAACTG	61	39	31	
	Probe	TGTTGATGACACTGCCA-GATGCGACGA	72	52	27	6FAM/TAMRA
<i>tdh</i>	Forward Primer	GTAAAGGTCTCTGACTTTT-GGACAAACC	62	43	28	
	Reverse Primer	AGTCATGTAGGATGTCAGC-CATTTAGTAC	60	41	29	
	Probe	CCGTACAAAGATGTTTATG-GTCAATCAGTATTCACAACG	71	38	39	VIC/TAMRA

*V. parahaemolyticus* isolates were obtained from the US Food and Drug Administration. Molecular characterization on these isolates has been conducted in our previous study that showed that these isolates have different pulsotype (Yeung et al., 2002). Other characteristics of these isolates are shown in Table 2. *V. alginolyticus*, and *V. vulnificus* were obtained from Hardy Diagnostic (Santa Maria, CA).

## RESULTS

Real-time PCR on *tlh* and *tdh* was conducted on 12 *V. parahaemolyticus* strains, 1 *V. alginolyticus* and 1 *V. vulnificus* strains. As expected, *V. alginolyticus* and *V. vulnificus* were negative for *tlh*- and *tdh*-PCR. All *V. parahaemolyticus* strains were positive for *tlh*. These results confirmed the primers and probes were specific for *V. parahaemolyticus*.

**Table 2.** Real-time and conventional PCR results from 14 different confirmed *Vibrio* isolates (actual quantitative  $C_T$  values not shown for clarity). All real-time PCR results were replicated at least once. Proper controls were used in all experiments. Conventional PCR results were determined previously by our lab.

<i>Vibrio</i> strains	Serotype	Source of isolation	<i>tlb</i> -PCR		<i>tdb</i> -PCR	
			Conventional <sup>2</sup>	Real-Time	Conventional	Real-Time
<i>V. alginolyticus</i>						
ATCC 17749	NA <sup>1</sup>		ND <sup>3</sup>	-	ND	ND
<i>V. vulnificus</i>						
ATCC 29307	NA		ND	-	ND	ND
<i>V. parahaemolyticus</i>						
FSL-Y1-001	O8	Food (clam)	+	+	-	-
FSL-Y1-002	O4:K8	Food (oyster)	+	+	+	+
FSL-Y1-005	O1	Food (oyster)	+	+	-	-
FSL-Y1-006	O5	Food (oyster)	+	+	-	-
FSL-Y1-010	O5:K15	Clinical	+	+	+	+
FSL-Y1-012	O4:K12	Clinical	+	+	-	-
FSL-Y1-013	O6:K18	Clinical	+	+	-	+
FSL-Y1-014	O4:K68	Clinical	+	+	+	+
FSL-Y1-016	O3:K6	Clinical	+	+	+	+
FSL-Y1-017	O3:K6	Clinical	+	+	+	+
FSL-Y1-021	O3:K6	Clinical	+	+	+	+
FSL-Y1-022	O3:K6	Clinical	+	+	-	-

<sup>1</sup> Not applicable

<sup>2</sup> Results from a previous study (Yeung et al., 2002)

<sup>3</sup> Not determined

The results for different *V. parahaemolyticus* strains were compared against previously published conventional PCR results (Table 2) to determine the sensitivity and specificity (Table 3). The values shown in Table 3 indicate false nega-

tive (sensitivity) and false positive (specificity) rates. Sensitivity and specificity for both genes was 100% except for specificity of *tdh* which was 88%. Specifically, *tdh* was detected in FSL-Y1-013 by real-time PCR but not by conventional PCR. We speculate that the primers used in real-time PCR may be more specific than those used in conventional PCR.

**Table 3.** Sensitivity and specificity of detecting *tlh* and *tdh* using real-time PCR as compared to using conventional PCR.

Gene	Sensitivity	Specificity
<i>tlh</i>	12/12 = 100%	2/2 = 100%
<i>tdh</i>	6/6 = 100%	7/8 = 88%

To determine the number of cells initially present in the reaction, a standard curve was constructed to correlate the threshold cycle ( $C_T$ ) value with varying concentration of DNA (and thereby cell number).  $C_T$  is the number of cycle required to generate sufficient fluorescent signal to reach a pre-defined threshold level. The lower the amount of DNA (or cell) in the sample, the higher the  $C_T$  value. Figure 2 shows results from a representative standard curve experiment.

The limit of detection of *tlh* and *tdh* were 9.16 and 6.13 pg of DNA, respectively. These amounts of DNA corresponded to  $2.2 \times 10^3$  and  $1.5 \times 10^3$  cfu/mL, respectively.

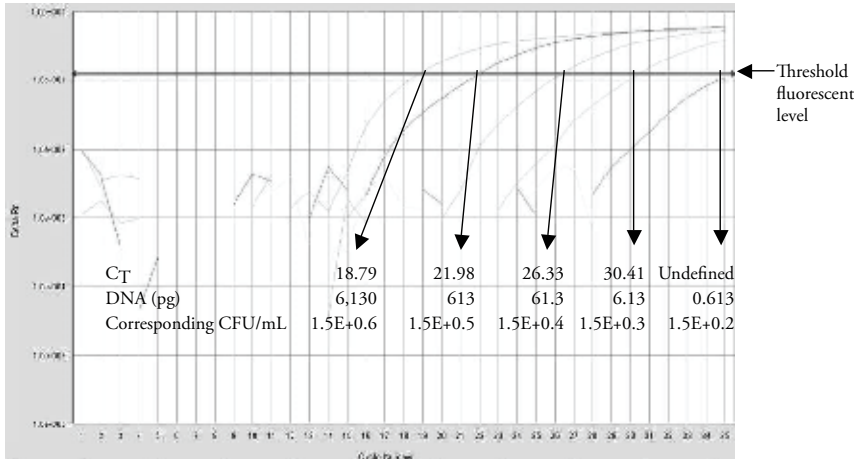


**Figure 2.** A standard curve using the log of threshold cycle ( $C_{T}$ ) values was constructed for *tdh*. The negative control has no amplification. The *tdh* gene had a  $R^2$  value from the standard curve of 0.99.

## CONCLUSIONS

A rapid molecular detection method using real-time PCR was successfully developed and optimized for the detection of two *V. parahaemolyticus* genes, *tlh* and *tdh*. With the optimized real-time PCR assay, our next step is to determine its sensitivity and specificity using food samples. Future research directions could include primers and probes designed for other pathogenic markers besides *tdh*, such as the Type III Secretion System (Park et al., 2004) to enhance the utility of this approach. Having the ability to provide timely and accurate results on the prevalence of pathogen is critical to maintain and improve the safety of our food supply.

## WORKS CITED

- Centers for Disease Control and Prevention. 2007. Preliminary FoodNet Data on the Incidence of Infection with Pathogens Transmitted Commonly Through Food --- 10 States, 2006. *Morb Mortal Wkly Rep.* 56:336-339.
- Honda, T., Iida T., Akeda Y., Kodama T. 2008. Sixty Years of *Vibrio parahaemolyticus* Research. *Microbe.* 3:462-466.

- Mackay, I., Arden, K., Nitsche, A. 2002. Survey and Summary: Real-time PCR in Virology. *Nucleic Acids Research* 30:1292-1305.
- Park, K., Ono, T., Rokuda, M., Jang, M., Okada, K., Iida, T., Honda, T. 2004. Functional Characterization of Two Type III Secretion Systems of *Vibrio parahaemolyticus*. *Infection and Immunity* 72:6659-6665.
- ProMED-mail. 2007. *Vibrio parahaemolyticus*, oysters - USA (WA): int'l aler. ProMED-mail 2007; 13 Aug: 20070813.2637. <<http://www.promedmail.org>>. Accessed 21 Jan 2008.
- Ward, L., Bej, A. 2006. Detection of *Vibrio parahaemolyticus* in Shellfish by Use of Multiplexed Real-time PCR with TaqMan Fluorescent Probes. *Applied and Environmental Microbiology*, 72:2031-2042.
- Yeung PS, Hayes MC, DePaola A, Kaysner CA, Kornstein L, Boor KJ. 2002. Comparative phenotypic, molecular, and virulence characterization of *Vibrio parahaemolyticus* O3:K6 isolates. *Applied and Environmental Microbiology* 68:2901-2909.
- Yeung, M., Boor, K. 2004. Epidemiology, Pathogenesis, and Prevention of Foodborne *Vibrio parahaemolyticus* Infections. *Foodborne Pathogens and Disease*. 1:74-88.

# DROP IMPACT DYNAMIC RESPONSE STUDY OF JEDEC JESD22-B111 TEST BOARD

Michael Krist, Andrew Farris, Nicolas Vickers, Student Authors  
Dr. Jianbiao Pan, Research Advisor

## ABSTRACT

Mobile and handheld electronic devices are prone to being dropped. This drop event may result in failure of solder joints inside these devices. The need for RoHS compliant boards coupled with the demand for reliable electronics has resulted in the development of the JEDEC Standard JESD22-B111 to standardize the method of drop testing surface mount electronic components. However, there has been little study on the effects of additional mass on the board and rigidity of the board on drop test reliability. This paper examines the drop impact dynamic responses of the JEDEC JESD22-B111 board. Of interest are the effects of an attached cable and rigidity of the board on the peak acceleration at differ-

ent locations of the board. Fifteen 0.5 mm pitch CSPs were assembled on the board using Sn3.0Ag0.5Cu lead free solder. The drop test was conducted using a Lansmont M23 TTSII Shock Test system. A half-sine shock impact pulse of 1500 G with 0.5 ms duration was applied to the drop table where the test vehicle was mounted. Two accelerometers were used to monitor the peak acceleration with one placed on the drop table and the other on the board at the component location. Statistical analysis showed that both the rigidity of the board and a cable attachment have an effect on the peak acceleration at individual component locations. Results show that the peak acceleration differs significantly at different component locations and the peak acceleration at some component locations are much higher than on the drop table. A cable attached to the board is shown to influence both peak acceleration and symmetry. A correlation between the peak acceleration and the number of drops until component failure was assessed.

## INTRODUCTION

Handheld electronic devices are becoming ubiquitous across the world. These devices, such as cellular phones, personal digital assistants (PDAs), and MP3 players are prone to be dropped in the device's usable lifetime. This drop event may lead to full or partial failures of the solder joints inside the device. Recently the European Union (EU) Restriction of Hazardous Substances (RoHS) and other countries' lead-free directives banned the use of lead in consumer electronics products. There are many lead-free solder alloys that have been developed, such as SnAg, SnBi, SnCu, SnAgBi, and SnAgCu. Among the developed lead-free solder materials, SnAgCu alloy is considered by the electronics industry to be a standard alternative to eutectic tin-lead solder [1].

There has been a significant amount of research done in the last few years on drop impact reliability [2, 3]. The JEDEC standard JESD22-B111 [4] for the board level and related standards [5, 6] for subassembly level have been developed for handheld electronics drop testing. Much research has been dedicated to dynamic responses such as strain conditions [2, 7, 8] and validating finite element analysis (FEA) and numerical models [7, 9, 10]. In drop impact studies, an

accelerometer was typically placed on the drop test table [8, 11] to monitor peak acceleration and duration of the impact pulse or on the center of a test board to measure board-level acceleration pulse [12, 13]. However, the dynamic board response at all component locations has not been adequately studied.

The rigidity of the test board and how the board was mounted on the drop table may significantly affect the peak acceleration at the component level given the same input pulse on the drop table. There has been little study on the effects of additional mass due to a cable attachment and/or the rigidity of the board on drop test reliability. The purpose of this study is to investigate the effect of an attached cable and the rigidity of the board on the peak acceleration at different component locations of a JESD22-B111 compliance test board. A correlation between the peak acceleration and the number of drops-to-failure was assessed.

## DESIGN

Experiments were designed to investigate the effects of two different input factors on the peak acceleration at different locations of a test board. The input factors were: 1) with or without a cable attached to the board, and 2) the rigidity of the board. No cable is attached to the board during the drop testing if the post-drop resistance measurement method is used to detect failure of solder joints, whereas a cable is attached in the in-situ high-speed data acquisition method.

The rigidity of the board has four levels: 1) blank board, 2) populated board with no edge-bond, 3) populated board with acrylic edge-bond, and 4) populated board with epoxy edge-bond. The blank board means a bare board without components assembled. The populated board with no edge-bond means a board with components assembled, but no edge bonding applied. The components, the test vehicle, and edge bond materials were the same as used in our previous study [1]. Figure 1 shows an example of an edge-bonded Chip Scale Package (CSP).

Figure 2 shows the drop test setup. The test vehicle was mounted in a horizontal position with the components facing downward, which is the most severe orientation [9]. Fifteen 0.5 mm pitch CSPs were assembled on a JESD22-B111 compliance test board using Sn3.0Ag0.5Cu lead free solder. The test board is an

eight-layer FR4 material board with a size of 132 mm by 77 mm and a thickness of 1 mm.

The drop test was conducted using a Lansmont M23 TTSII Shock Test system. A half-sine shock impact pulse of 1500 G with 0.5 ms duration, or a 2900 G with 0.3 ms was applied to the drop table where the test vehicle was mounted. Two accelerometers were used, with one accelerometer placed on the drop table to monitor the peak acceleration and duration of the input pulse, and the other on the component location to measure peak acceleration at that location as shown in Figure 2.

There are 15 component locations on a board. The peak acceleration at each location was measured. Thus, there are 120 treatments total (2 levels of the use of cable times 4 levels of board rigidity times 15 component locations). Each experimental treatment was replicated twice. Therefore, a total of 240 drops were conducted. To reduce the expected degradation effect on the board rigidity due to continued bending, eight boards were used in this experiment, two for each level of board rigidity. The order of testing with and without cable was alternated between the two boards for each rigidity level.



**Figure 1.** An example of an edge-bonded CSP.

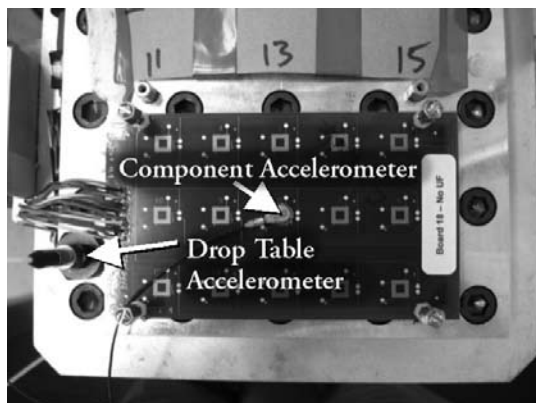
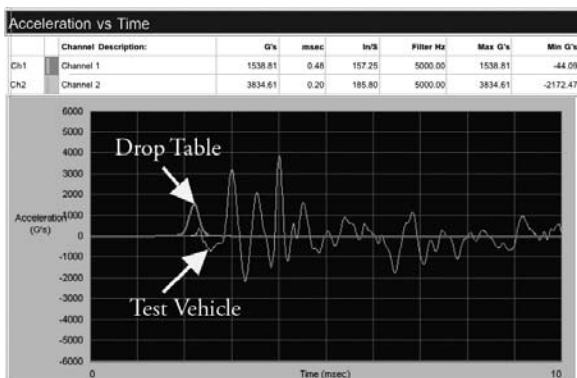


**Figure 2.** Test vehicle with one accelerometer on a component location and the other on the drop table.

## DATA ANALYSIS

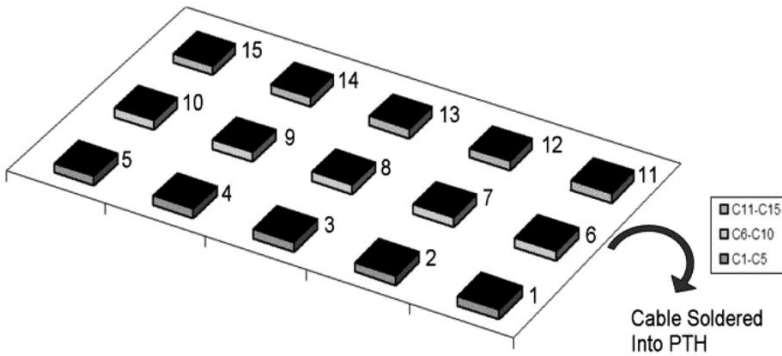
### Local Acceleration Results

Figure 3 shows an example of the acceleration responses of both the drop table and a component location at the test vehicle during a 1500 G drop. The half-sine response was that of the drop table, and the larger cyclic response was a component location at the test vehicle. It is clearly shown that the acceleration experienced by the test vehicle was completely different from that at the drop table. The test vehicle vibrated after the impact and experienced higher peak acceleration than the drop table. The peak acceleration at the test vehicle occurred at a later time than at the drop table.



**Figure 3.** Dynamic acceleration responses of drop table and test vehicle.

An overview of the placement of each component on the board in relation to the cable is shown in Figure 4. The average peak acceleration at the 15 component locations for blank board, populated board with no edge-bond, populated board with epoxy edge-bond, and populated board with acrylic edge-bond are shown in Figures 5–8, respectively. The peak acceleration of each component location without a cable attached is shown in the left side and the peak acceleration with a cable is shown in the right side of Figures 5–8. A bold horizon line in these four figures represents the input acceleration of 1500 G. The results indicate the significant effect of the cable on local accelerations. In every case, the cable reduces the overall peak acceleration and disrupts symmetry. The reduction of the peak acceleration may be due to the additional mass from the cable. The mass of the attached cable also shifts the center of mass of the test board, which disrupts the symmetry of acceleration behavior. It is also evident that the populated boards experience less acceleration than the blank board due to increased rigidity and mass.



**Figure 4.** Cable in relation to component locations.

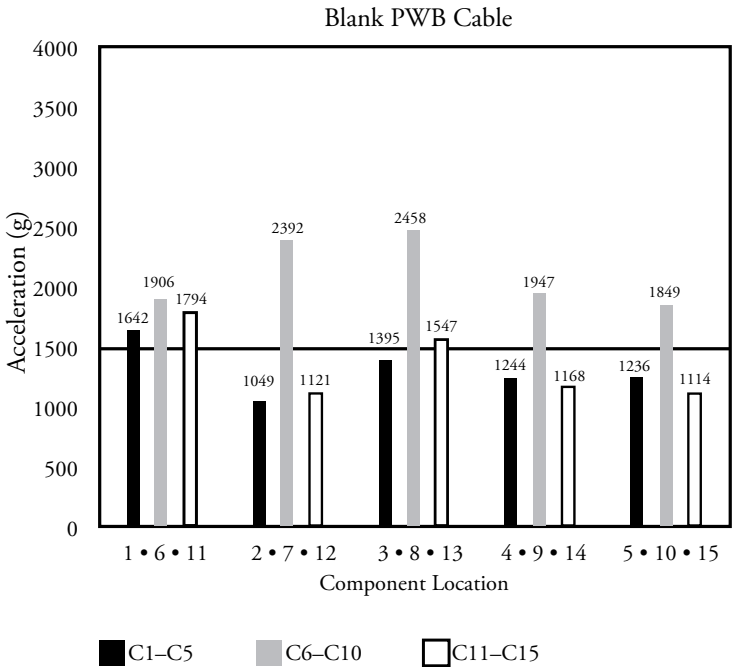
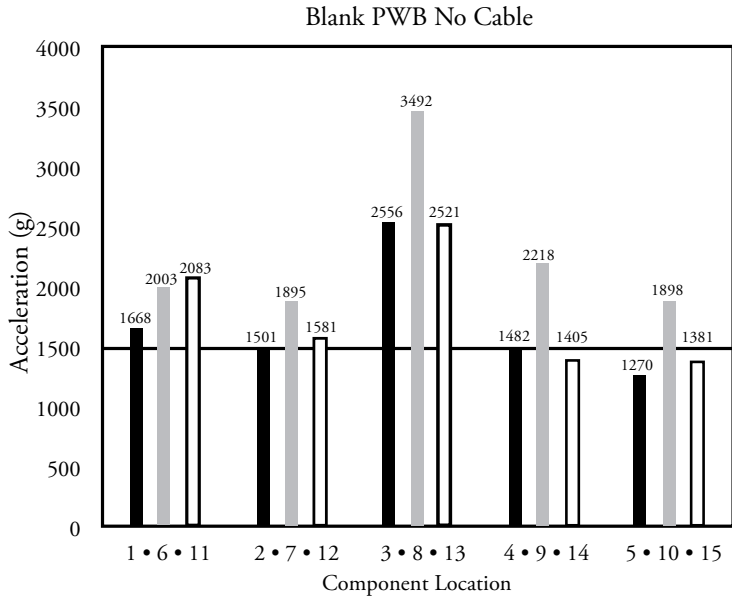


**Figure 5.** Accelerations on blank board with no cable and with cable.

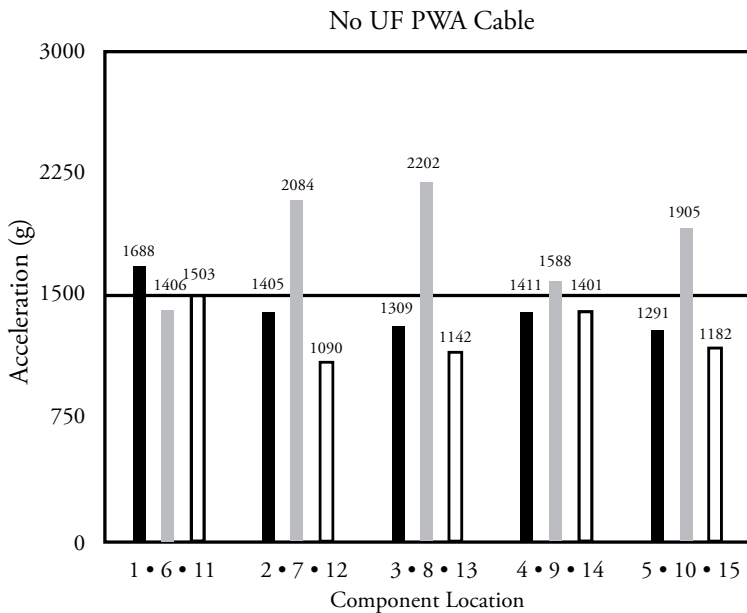
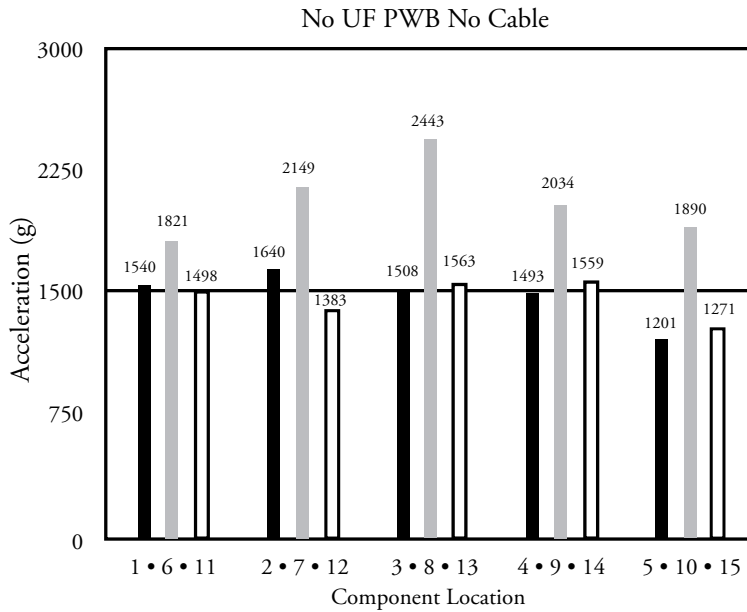


**Figure 6.** Accelerations on populated board with no cable and with cable.

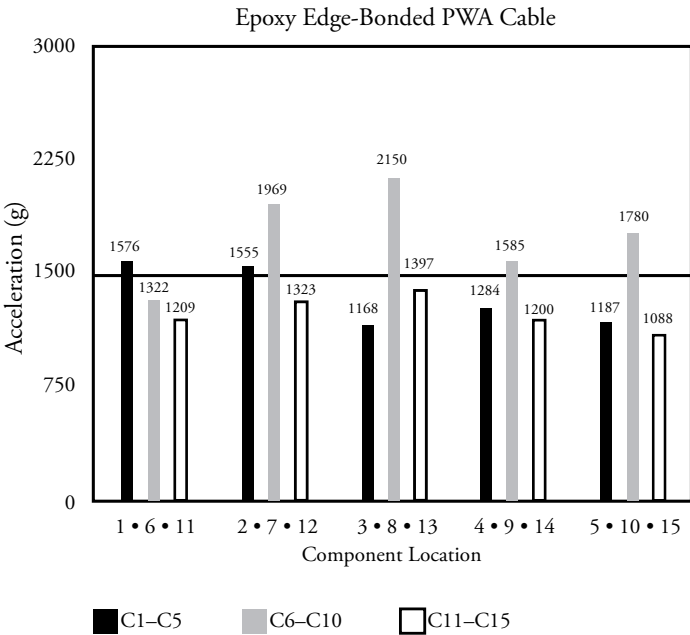
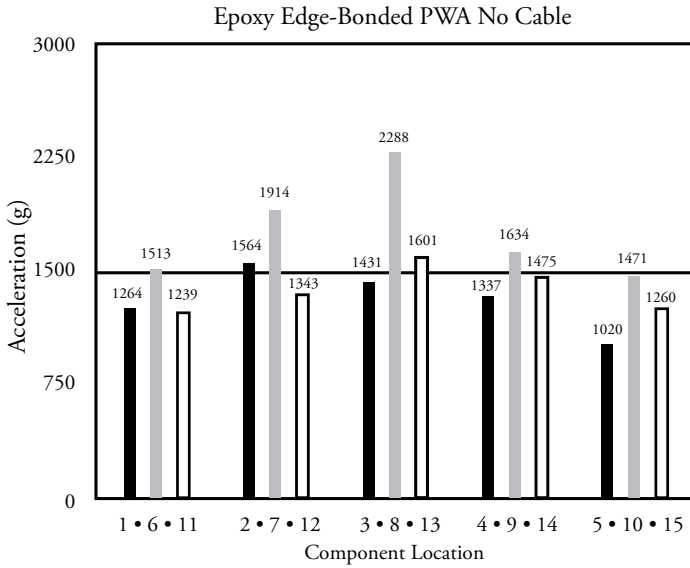


**Figure 7.** Accelerations on epoxy edge-bond populated board without cable and with cable.

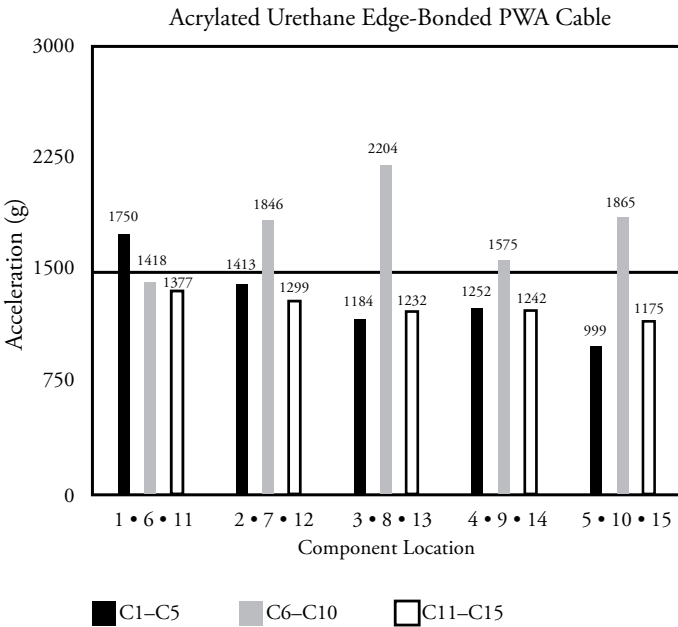
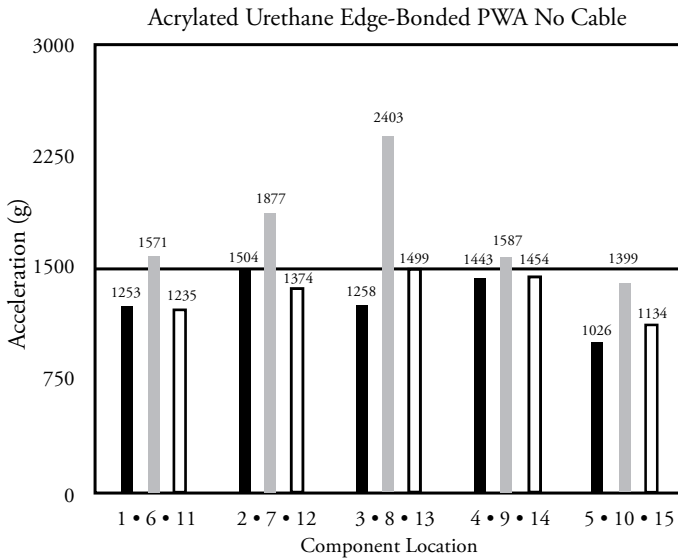


**Figure 8.** Accelerations on acrylic edge-bond populated board with no cable and with cable.

## Statistical Analysis

Analysis of variance (ANOVA) was used to determine the effects of the cable and board rigidity on the peak acceleration at individual component locations. Figure 9 shows the effect of the cable. The component locations filled with dark color are the locations in which the cable has a statistically significant effect, at a 95% confidence level, on peak acceleration on that location. The figure shows that component locations 2, 3, 4, 6, 8, 9, 12, 13, and 14 all experienced significantly different accelerations when a cable was attached compared to when no cable was attached. At each of the significant locations, the component experienced less peak acceleration with the cable attached.

Figure 10 shows the effect of board rigidity on the peak acceleration at different locations. It shows that the rigidity of the board has statistically significant effect on locations 3, 6, 8, 9, 11, 13, and 14. In these locations, the populated board experienced significantly less peak acceleration than the blank board. However, there is no statistically significant difference in peak acceleration between the populated board without edge bond and the populated board with edge bond across all tested locations. There is also no significant difference in peak acceleration at every location of the board between the epoxy edge-bond and acrylic edge-bond. Previous studies have found that drop test reliability of solder joints without edge-bond is much poorer than solder joints with edge-bond [1, 14]; however, no significant difference exists in peak accelerations between these two cases at any component location.

To understand the effect of a cable and the rigidity of a board on the peak acceleration according to JEDEC defined symmetry group locations, as shown in Figure 11, another ANOVA was analyzed. Since the JEDEC standard drop test induces a complex strain pattern across the test board, JEDEC recommendations divide the components on the test board into six groups (A-F) that are expected to have similar failure rates due to board location symmetry [1], [4]. This ANOVA test was conducted by grouping the components according to their JEDEC grouping and re-analyzing the same data. The peak acceleration at the different JEDEC defined locations is shown in Figure 12. It is interesting to note

that group location E has a lower peak acceleration than group locations C and D, although JEDEC specifies group location E having greater strain [4].

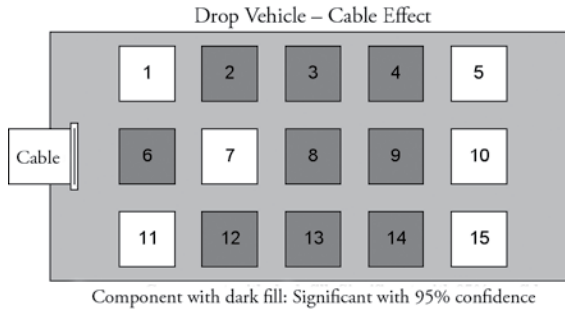


**Figure 9.** Effect of a cable on peak acceleration of different component locations. The component locations filled with dark color are the locations in which the cable has a statistically significant effect on peak acceleration on that location.

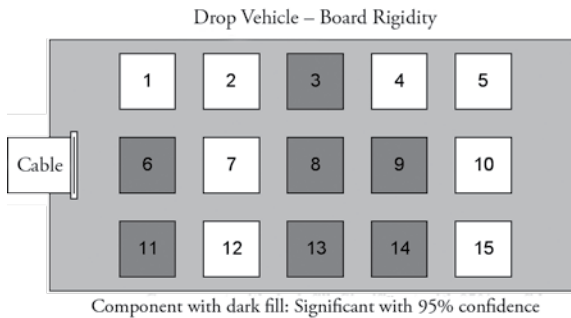


**Figure 10.** Effect of the rigidity of a board on peak acceleration of different component locations. The component locations filled with dark color are the locations in which the rigidity of a board has a statistically significant effect on peak acceleration on that location.

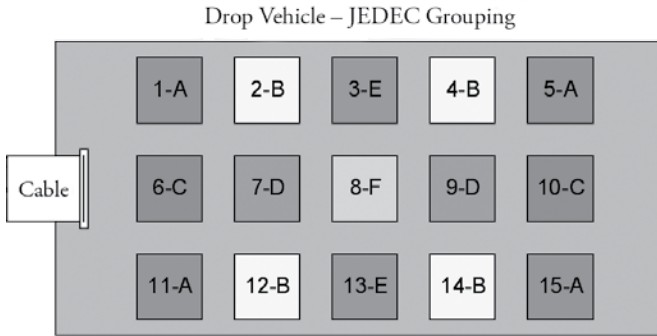


**Figure 11.** JEDEC defined symmetric component location groups.

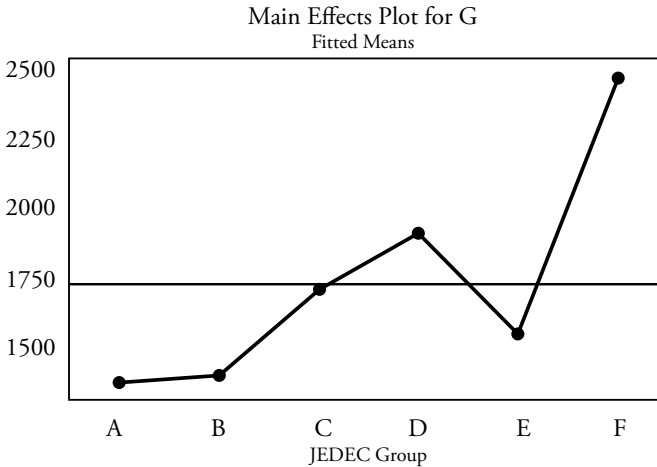


**Figure 12.** Main effects of peak acceleration by JEDEC defined location.

### Relationship between Reliability and Component Location

To assess whether a high peak acceleration results in the failure of solder joints in a drop impact test, the number of drops-to-failure for boards with edge-bonding at each component location group defined by JEDEC [2] was analyzed. All data of drops-to-failure at each component location have been reported in our previous study [1].

Because many repetitive drops are required to completely fail drop tested devices, many studies stop the drop testing process after a preselected number of

failures occur, or after a certain number of drop impacts. Statistically, the data gathered from this testing type is known as right-censored. In the case of reliability analysis with right-censored data, a predetermined number of failures would typically be used to obtain an accurate estimate of a failure trend [15]. In this study, both the censored and non-censored data were analyzed using Minitab's Reliability/Survival Analysis functions. Since the number of drops-to-failure follows the Weibull distribution, cumulative failure plots were generated for both the 1500 G with 0.5 ms duration impact and the 2900 G with 0.3 ms duration impact, as shown in Figures 13 and 14, respectively. Reliability analysis was performed for each component location group based on the JEDEC board grouping (A-F).

Figure 13 shows that group E and F failed at the fastest rate at 1500 G. Note that Group F has a different shape than the other groups. This may be due to a relatively low ratio of failed data to censored data. Groups A, B, C, and D have similar failure rates, with B showing the fastest failure rates of those four component groups. This does not correlate with the peak acceleration experienced by the location of component group. JEDEC group D, which experienced the second highest peak acceleration, had the slowest failure rate in the 1500 G impact. Conversely, JEDEC group E, which experienced relatively low peak acceleration, had the second fastest failure rate in the 1500 G impact. Figure 14 shows a much more consistent pattern of failure rates under 2900 G impact. This is most likely attributed to the higher ratio of failed to censored data. Again, groups E and F have the highest failure rates of all the groups. This analysis indicates that a high local acceleration does not necessarily correlate to a low number of drops-to-failure.

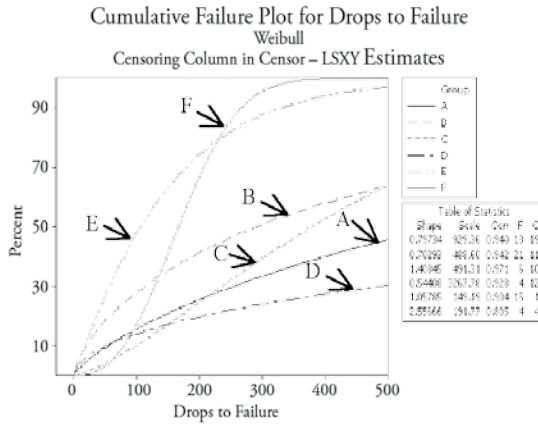


**Figure 13.** Cumulative failure plot for drops to failure of each group at 1500 G.

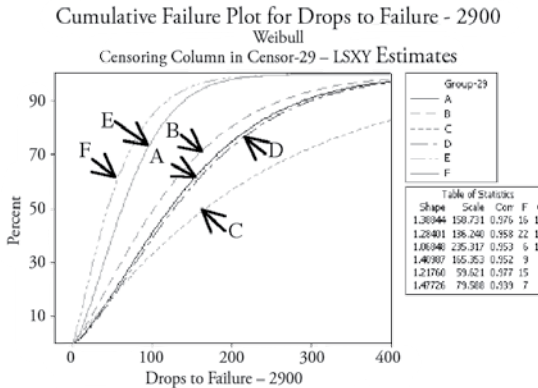


**Figure 14.** Cumulative failure plot for drops to failure of each group at 2900 G.

## CONCLUSIONS

The following conclusions can be drawn from this research:

1. A cable or other additional mass attached to a drop test board significantly affects the peak value and symmetry of acceleration at many component locations on the board.
2. Higher local peak acceleration does not directly correlate to a lower number of drops-to-failure in that location.

3. The peak acceleration at every component location on the populated board without edge-bond is similar to that on the populated board with acrylic edge-bond or epoxy edge-bond, therefore the board rigidity is similar, but the drop test reliability of solder joints without edge-bond is much poorer than solder joints with edge-bond.

## ACKNOWLEDGEMENTS

The authors would like to thank Mr. Jasbir Bath, Mr. Dennis Willie, Mr. David A. Geiger, and Dr. Dongkai Shangguan of Flextronics, Dr. Brian J. Toleno and Mr. Dan Maslyk of Henkel Technologies for technical support. The first author gratefully acknowledges the financial support from National Science Foundation through Cal Poly's Honors Program.

## WORKS CITED

- [1] A. Farris, J. Pan, A. Liddicoat, B. J. Toleno, D. Maslyk, D. Shangguan, J. Bath, D. Willie, D. Geiger, "Drop Test Reliability of Lead-Free Chip Scale Packages", *Proc. of 2008 IEEE ECTC*, pp. 1173-1180.
- [2] Y.S. Lai, P.C Yang, C.L. Yeh, "Effects of Different Drop Test Conditions on Board-Level Reliability of Chip-Scale Packages", *Microelectronics Reliability*, Vol. 48, No. 2, Feb. 2008, pp. 274-281.
- [3] J. Zhao, F. Liu, X. Zhou, H. Zhou, J. Jing, M. Zhao, "Improvement of JEDEC Drop Test in SJR Qualification through Alternative Test Board Design," *Proc. of Electronic Components and Technology Conference*, May 2007, pp. 946-950.
- [4] JEDEC Standard JESD22-B111, "Board Level Drop Test Method of Components for Handheld Electronic products", JEDEC Solid State Technology Assoc, 2003.
- [5] JEDEC Standard JESD22-B104-C, "Mechanical Shock," JEDEC Solid State Technology Assoc, 2004.
- [6] JEDEC Standard JESD22-B110A, "Subassembly Mechanical Shock," JEDEC Solid State Technology, 2004.
- [7] C.-L. Yeh, T.-Y. Tsai, Y.-S. Lai, "Transient Analysis of Drop Responses of Board-Level Electronic Packages using Response Spectra Incorporated with Modal Superposition," *Microelectronics Reliability*, Vol. 47, No. 12, 2007, pp. 2188-2196.
- [8] C.-L. Yeh, Y.-S. Lai, C.-L. Kao, "Evaluation of Board-Level Reliability of Electronic Packages under Consecutive Drops," *Microelectronics Reliability*, Vol. 46, No. 7, 2006, pp. 1172-1182.
- [9] J.E Luan, T.Y. Tee, E. Pek, C.T. Lim, Z. Zhong, J. Zhou, "Advanced Numerical and Experimental Techniques for Analysis of Dynamic Responses and Solder Joint Reliability During Drop Impact", *IEEE Transactions on Component and Packaging Technologies*, Vol. 29, No. 3, Sept. 2006, pp. 449 – 456.

- [10] E. Wong and Y. Mai, "New Insights into Board Level Drop Impact," *Microelectronics Reliability*, Vol. 46, No. 5-6, May 2006, pp. 930-938.
- [11] Y.S. Lai, P.F. Yang, C.L. Yeh, "Experimental Studies of Board-Level Reliability of Chip-Scale Packages Subjected to JEDEC Drop Test Condition", *Microelectronics Reliability*, Vol. 46, No. 2, 2006, pp. 645-650.
- [12] L. Zhu and W. Marcinkiewicz, "Drop Impact Reliability Analysis of CSP Packages at Board and Product Levels through Modeling Approaches," *IEEE Transactions on Components and Packaging Technologies*, Vol. 28, No. 3, 2005, pp. 449-456.
- [13] D. Chong, K. Ng, J. Tan, P. Low, J. Pang, F. Che, B. Xiong, L. Xu, "Drop Impact Reliability Testing for Lead-Free & Leaded Soldered IC Packages", *Proc. of 2005 IEEE Electronics Components and Technology Conference*, pp. 622-629.
- [14] B. Toleno, D. Maslyk, T. White, "Using Underfills to Enhance Drop Test Reliability of Pb-free Solder Joints in Advanced Chip Scale Packages", *Proc. of 2007 SMTA Pan Pacific Symposium*, 2006.
- [15] G. Wasserman, "Reliability Verification, Testing, and Analysis in Engineering Design", New York: Marcel Dekker, 2003

# THE EXPRESSION OF ALKALINE PHOSPHATASE IN COLONIAL ASCIDIANS

Katherine Januszewicz, Heidi Swangler, Student Authors  
Dr. Elena Keeling, Research Advisor

## ABSTRACT

The goal of this project was to better understand anatomical and physiological characteristics of the colonial ascidian, *Botrylloides violaceus*, a marine tunicate species. One reason for studying *Botrylloides violaceus* is that it is an invertebrate that is especially closely related to vertebrates. *Botrylloides violaceus* has the ability to reproduce sexually and asexually (through a process called “budding”), and to regenerate an entire body from stem cells in the circulatory system. The regeneration process is not well understood and does not occur in the better studied species of solitary ascidians. To better understand the process of regeneration, this study focused on the expression of the enzyme alkaline phosphatase. This

enzyme has been used as a marker for stem cells, which differentiate into other cells, a vital part of regeneration. However, the enzyme is expressed in other tissues and its specific role in development is still unknown. To better understand the anatomy of a *Botrylloides violaceus* colony, tissue sections stained with hematoxylin and eosin were analyzed. To perform a preliminary examination of the role of alkaline phosphatase in development, colony tissue sections were stained for the expression of the enzyme. Expression was seen in adult endodermal tissue and in scattered cells within the circulatory system.

## BACKGROUND

The colonial ascidian *Botrylloides violaceus* is a filter-feeding marine tunicate species belonging to the phylum Chordata. Tunicates are very closely related to vertebrates, and although it is debated, some scientists argue that they are in fact vertebrates' closest relatives (Delsuc et al. 2006). Therefore, understanding more about regeneration in tunicates may shed light on regeneration in vertebrates. Colonial ascidians form colonies of identical zooids, or adults, from a single settled larva (Burighel & Cloney, 1997). The colony shares a circulatory system, but each zooid has its own organs and reproductive capabilities.

*Botrylloides violaceus* has the ability to reproduce both sexually and asexually (through a process called “budding”), and it also has the ability to regenerate an entire body from stem cells in the circulatory system (Manni & Burighel, 2006; Rinkevich et al., 1995). Sexual reproduction occurs seasonally. Zooids develop testes and ovaries in order to form sperm and eggs. Once fertilization occurs, an embryo is produced which will develop into larvae in a brood chamber within the colony. These larvae are released and are then free to start a new colony. During asexual reproduction, a bud forms from the body wall and becomes an identical copy of the parent (Oka & Watanabe, 1957). If all body parts are removed, leaving only the circulatory system, the organism can regenerate itself entirely from some subset of circulatory blood cells. These cells must be stem cells since they have the ability to give rise to all differentiated cell types (Rinkevich et al., 1995). There are many questions about the similarities and differences between asexual

reproduction and regeneration, how regeneration is regulated, and which cells are the stem cells.

Alkaline phosphatase is a membrane-bound enzyme widely expressed across different species and developmental stages, and it has many different biochemical functions. It plays a major role in the hydrolysis of phosphates and also regulates the transport of several different compounds, such as calcium, fats, and proteins. Alkaline phosphatase is expressed in proliferating cells and in cells with a high rate of metabolism (Iida et al., 2007). Many questions have arisen about this enzyme's role in the process of proliferation, cell substrate adhesion, and also whether this enzyme is active in inducing differentiation of cells (Hui et al., 1996).

Alkaline phosphatase is commonly found in the intestine of numerous organisms and has been found in early developmental stages of the endoderm, a tissue that gives rise to the gut. This pattern of expression has been seen in solitary ascidians, for example (Whittaker, 1990). Alkaline phosphatase has also been found on the membranes of germ cells and stem cells (Akhmadieva et al., 2007; Iida et al., 2007). This is of great importance because there are still questions surrounding the morphological characteristics of stem cells. The expression of alkaline phosphatase by stem cells has mostly been studied in mammals, but two recent studies of species in the botryllid family have revealed the expression of alkaline phosphatase in stem cells of colonial ascidians (Akhmadieva et al., 2007; Rinkevich et al., 2007). Using light and electron microscopy, these studies revealed prospective stem cells that appeared to be hemoblasts; they were characterized as having a high nucleus to cytoplasm ratio, dense hematoxylin staining, and a small, round cell shape. In one of these studies, an ascidian showed differentiation of hemoblasts into germ cells (Akhmadieva et al., 2007). These findings give rise to more questions concerning the specific subpopulation of hemoblasts that are stem cells.

The objective of this project was to better understand the anatomy of the colonial ascidian, *Botrylloides violaceus*, as well as to examine its cellular expression of alkaline phosphatase. Neither endoderm expression nor stem cell expression of

alkaline phosphatase has been studied in *Botrylloides violaceus*, and the enzyme's role in the organism is not understood. In this project, the first steps were taken toward examining this question. The basic tissue stain hematoxylin and eosin was performed on thin colony slices of *Botrylloides violaceus* in order to highlight important anatomical structures. Other colony tissue slices were stained for the presence of alkaline phosphatase.

## METHODS

*Botrylloides violaceus* tissue samples, embedded in polyester wax, were used to prepare slides with serial sections of the organism. Using a microtome, 7-micron tissue slices were cut and mounted onto gelatin-subbed slides. The slides were allowed to air-dry for 48 hours and were then placed in the refrigerator until staining (Presnell & Schreiberman, 1997).

To perform a basic hematoxylin and eosin tissue stain, subbed slides with mounted tissue sections were treated with pure ethanol to remove the wax and then gradually rehydrated through an ethanol series of decreasing strengths. After staining with hematoxylin for four minutes, the slides were rinsed with deionized water and placed in Scott's Solution (0.02 M NaHCO<sub>3</sub> and 0.16 M MgSO<sub>4</sub>), followed by an eosin counterstain for three minutes. The stained slides were gradually dehydrated in another ethanol series of increasing strengths, followed by toluene for two minutes and mounted in Permount (Presnell & Schreiberman, 1997). Hematoxylin stains the nucleus of cells blue and eosin stains the cytoplasm of cells pink.

To test for the expression of alkaline phosphatase, several slides with mounted tissue sections of *Botrylloides violaceus* colonies were rehydrated through an ethanol series of decreasing strengths, and placed in phosphate buffer saline (PBS). The slides were then placed in Buffer 3 pH 8 (100 mM Tris-Cl pH 8.0, 100 mM NaCl, and 50 mM MgCl<sub>2</sub>), followed by Buffer 3 pH 9.5 (100 mM Tris-Cl pH 9.5, 100 mM NaCl, and 50 mM MgCl<sub>2</sub>). The tissue sections on the slides were covered with Buffer 3 pH 9.5, NBT, and BCIP, and then developed in a dark, moist chamber. BCIP is a colorless compound that contains a phosphate group.

If alkaline phosphatase is present, it will cleave the phosphate group from BCIP. NBT is a yellow compound that will then bind with the dephosphorylated BCIP to produce a blue precipitate. The presence of blue precipitate indicates alkaline phosphatase expression. The slides were then rinsed with PBS and dehydrated through an ethanol series of increasing strengths. They were counterstained with eosin for approximately two minutes and mounted in Permount (adapted from Whittaker, 1990).

## RESULTS

The hematoxylin and eosin stain highlighted the tissues, as seen in Figures 1 and 2, although very little eosin counterstain was observed. This stain highlighted major anatomical structures within a *Botrylloides violaceus* colony. In Figure 1 the colony is seen in cross-section revealing three adjacent adult zooids, or individual bodies, across the bottom of the figure (a). Cross-sections of two buds, flanking the center zooid, are visible (b). Cross-sections through blood vessels are also seen (c). Within each individual zooid, the pharynx or branchial basket is seen (a). In order to feed, water filters into the pharynx through the oral siphon of a zooid and food is caught by cilia on the endostyle (indicated by white arrows), where the food is taken in. A close-up view of an endostyle and cilia of an individual zooid can be seen in Figure 2.

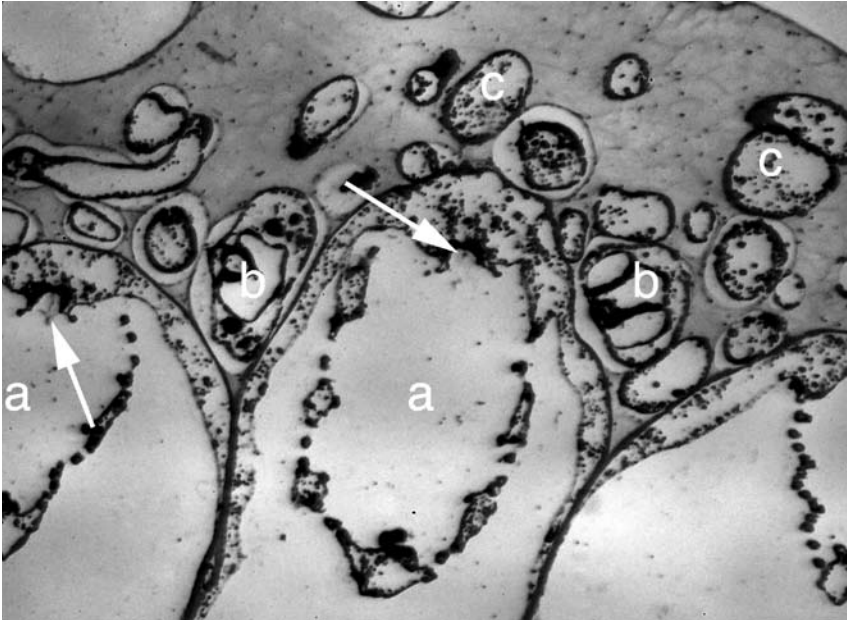


**Figure 1.** Hematoxylin and eosin stain of a *Botrylloides violaceus* colony section. (a) adult zooid branchial basket, (b) buds showing earlier stages of development, (c) cross sections through blood vessels, Arrows: endostyles in adult zooid.

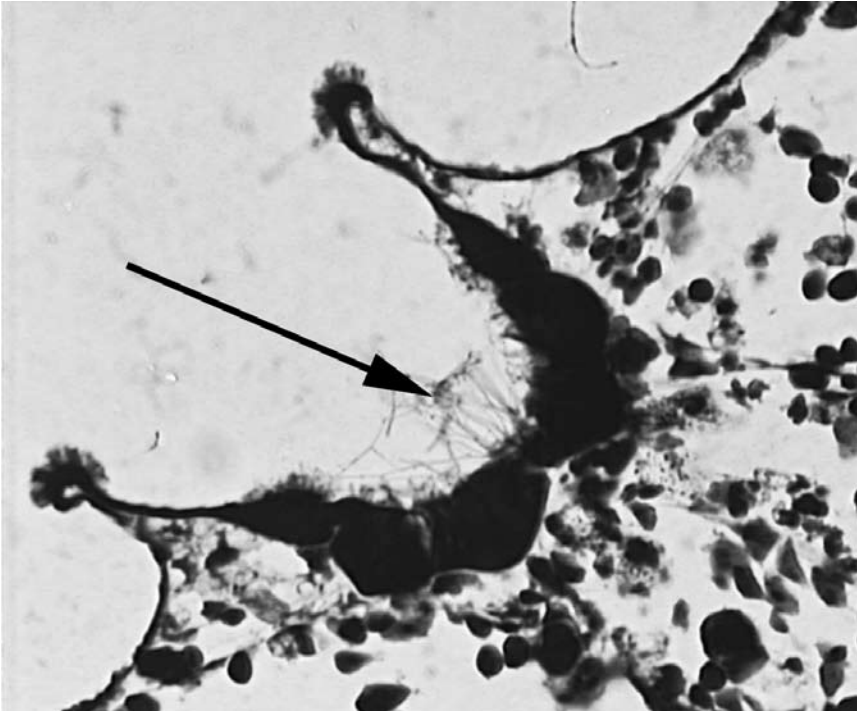


**Figure 2.** Hematoxylin and eosin stain of a *Botrylloides violaceus* colony section—close-up view of endostyle within pharynx of adult zooid. Cilia are indicated by arrow.

Alkaline phosphatase expression was indicated by the brown and blue pigment seen within the cells. Figure 3a shows extensive expression on a large stomach from an adult zooid. Figure 3b shows the same adult stomach showing expression, and above this stomach a smaller, less developed stomach showing no expression is seen. This smaller stomach appears to be that of a large bud. Figure 3c shows a brood chamber surrounding an embryo extensively expressing alkaline phosphatase activity. Figure 3d shows expression in scattered cells in the circulatory system, some of which may be stem cells. It is important to note that expression is not seen in all circulating cells.

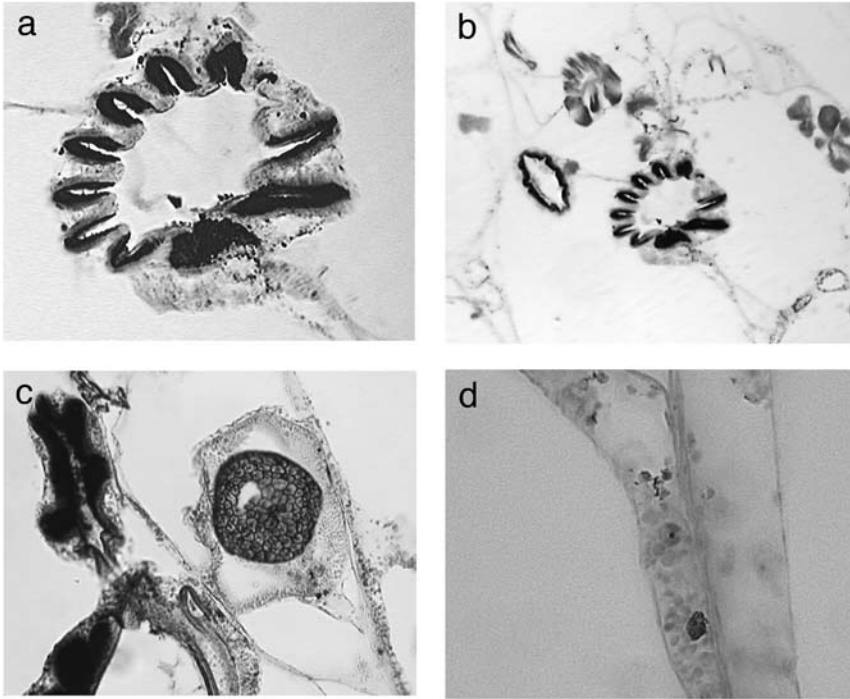


**Figure 3.** Alkaline phosphatase expression in *Botrylloides violaceus* tissue sections. (a) Stomach of a mature zooid showing positive staining for alkaline phosphatase. (b) Colony section showing the stomach of a mature zooid, showing positive staining for alkaline phosphatase, and the smaller stomach of a large bud, showing a lack of staining for alkaline phosphatase. (c) Colony section showing a brood chamber with an embryo stained positively for alkaline phosphatase. (d) Blood vessel showing scattered blood cells positively staining for alkaline phosphatase.

## DISCUSSION

The purpose of this project was to section tissues of *Botrylloides violaceus*, perform a basic tissue stain on the sections to better understand the colonial anatomy, and stain for the activity of alkaline phosphatase. The hematoxylin and eosin staining procedure allowed the anatomy of the colonial ascidians to be viewed and better understood. However, the eosin counterstain did not stain the tissues well. There was no pink color to offset the dark purple of the hematoxylin stain. Increasing the time of incubation in eosin up to five minutes produced the same results. It is possible that the *Botrylloides violaceus* tissue has slightly different properties than

other tissues successfully stained with hematoxylin and eosin. More research must be done to fully understand the reason for minimal eosin staining.

An effective staining procedure for the alkaline phosphatase was successfully developed. With this procedure, tissue sections of colonies were stained, and structures within the colonies were compared for the expression of alkaline phosphatase. There were different patterns of expression observed in the various tissues, especially in the developing endoderm. It appears that smaller stomachs of the buds did not show expression of the enzyme, whereas the larger, more mature stomachs did. This could potentially mean that there are different amounts of expression at varying developmental stages of the gut in colonial ascidians. This is interesting because it suggests a potential difference in alkaline phosphatase expression between solitary ascidians and colonial ascidians. In solitary ascidians, alkaline phosphatase expression has been seen in the very early embryo in cells fated to give rise to the gut, before any visible differentiation occurs (Whittaker, 1990). It is also possible that the pattern of expression differs between embryonic development of the endoderm and its development during asexual budding. To investigate these possible differences further, more stomach sections at different stages of development need to be examined in colonies, and it should be determined at what stage of development or size threshold the expression is first seen. Examination of more sections will allow confirmation that there is a genuine size difference rather than simply artifact of sectioning angle. In addition, expression of alkaline phosphatase in the stomachs of embryos and larvae should be examined.

Scattered blood cells within the tissue also showed varying amounts of alkaline phosphatase expression. In the future, a closer examination of the expression within the circulatory system will be made to identify the specific cell types that express alkaline phosphatase. Based on previous studies (Akhmadiyeva et al., 2007), it is predicted that alkaline phosphatase is expressed in hemoblasts in *Botrylloides violaceus*. It is not known whether all or only a subset of hemoblasts show expression, nor is it known whether other blood cells show expression. If only stem cells express alkaline phosphatase within the circulatory system, this

stain may serve as a marker to differentiate the stem cells from other circulating blood cells as it has in studies of other ascidians (Akhmadieva et al., 2007). A method of extracting blood from a live colony of *Botrylloides violaceus* will be developed in order to isolate these cells away from the surrounding tissue to make cell type identification easier and to clarify enzyme expression patterns. Finally, to confirm stem cell identity we will examine expression of other proteins indicative of stem cells and compare to alkaline phosphatase expression.

## ACKNOWLEDGEMENTS

Special thanks to the Honors Program for the opportunity and support for this project; Cal Poly Pier Manager Tom Moylan and Dr. Dean Wendt for their help with the collection of live species; the two anonymous reviewers of this paper for their constructive criticism; and especially Dr. Elena Keeling for her ongoing guidance and patience.

## WORKS CITED

- Akhmadieva, A.V., Shukalyuk, A.I., Aleksandrova, Y.N., & Isaeva, V.V. (2007). Stem cells in asexual reproduction of the colonial ascidian *Botryllus tubaratus* (Tunica: Ascidiacea). *Russian Journal of Marine Biology*, 33(3), 181-186.
- Burighel, P. & Cloney, R.A. 1997. Urochordata: Ascidiacea. *Microscopic Anatomy of Invertebrates, Volume 15: Hemichordata, Chaetognatha, and the Invertebrate Chordates*. 221-347.
- Delsuc, F., Brinkmann H, Chourrout D, Philippe H. (2006). Tunicates and not cephalochordates are the closest living relatives of vertebrates. *Nature*, 439, 965-968.
- Hui, M., Sukhu, B., & Tenebaum, H.C. (1996). Expression of tissue non-specific alkaline phosphatase stimulates differentiated behaviour in specific transformed cell populations. *The Anatomical Record*, 244: 423-236.
- Iida, M., Ihara, S., & Matsuzaki, T. (2007). Hair-cycle dependent changes of alkaline phosphatase activity in the mesenchyme and epithelium in mouse vibrissal follicles. *Development, Growth & Differentiation*, 49: 185-195.
- Manni, L. & Burighel, P. (2006). Common and divergent pathways in alternative developmental processes of ascidians. *BioEssays*, 28, 902-912.
- Oka, H. & Watanabe, H. (1957). Vascular budding, a new type of budding in botryllus. *Biological bulletin*, 112, 225-240.
- Presnell, J.K., & Schreibman, M.P. (1997). *Animal tissue techniques* (5th ed.), pp. 101-113. Baltimore: John's Hopkins University Press.
- Rinkevich, B., Shlemborg, Z., & Fishelson, L. (1995). Whole-body protochordate regeneration from totipotent blood cells. *Proceedings of the national academy of sciences*, 92, 7695-7699.
- Rinkevich, Y., Paz, G., Rinkevich, B., & Reshef, R. (2007). Systemic bud induction and retinoic

acid signaling underlie whole body regeneration in the urochordate *Botrylloides leachi*.  
*Public Library of Science*, 5(4), 900-913.

Whittaker, J.R. (1990). Determination of alkaline phosphatase expression in endodermal cell lineages of ascidian embryo. *Biological bulletin*, 178, 222-230.

# CONTRIBUTING STUDENTS

**Jenna Arruda**, Biochemistry

**Dustin Blackwell**, Aerospace Engineering

**Bert David Copsey**, Mechanical Engineering

**Andrew Farris**, Computer Engineering

**John Hupton**, Electrical Engineering

**Roberg Hursig**, Electrical Engineering

**Katherine Januszewicz**, Biological Science

**Jessica Kiefer**, Electrical Engineering

**Michael Krist**, Industrial Engineering

**Benjamin Kwittken**, Biological Science

**Evan Markegard**, Microbiology

**Matt Schlutz**, Electrical Engineering

**Scott Seims**, Electrical Engineering

**Heidi Swangler**, Biological Science

**Nicolas Vickers**, Materials Engineering

## CONTRIBUTING FACULTY AND STAFF

**Dr. Jennifer Carroll**, Chemistry & Biochemistry

**Dr. Katharina Gillen**, Physics

**Dr. Elena Keeling**, Biological Sciences

**Dr. Jianbiao Pan**, Industrial & Manufacturing Engineering

**Dr. John Saghri**, Electrical Engineering

**Dr. Emily N. Taylor**, Biological Sciences

**Dr. Marie Yeung**, Biological Sciences